

Relaxivity of manganese ferrite nanoparticles

Peters, Joop A.

DOI

[10.1016/j.pnmrs.2020.07.002](https://doi.org/10.1016/j.pnmrs.2020.07.002)

Publication date

2020

Document Version

Final published version

Published in

Progress in Nuclear Magnetic Resonance Spectroscopy

Citation (APA)

Peters, J. A. (2020). Relaxivity of manganese ferrite nanoparticles. *Progress in Nuclear Magnetic Resonance Spectroscopy*, 120-121, 72-94. <https://doi.org/10.1016/j.pnmrs.2020.07.002>

Important note

To cite this publication, please use the final published version (if applicable). Please check the document version above.

Copyright

Other than for strictly personal use, it is not permitted to download, forward or distribute the text or part of it, without the consent of the author(s) and/or copyright holder(s), unless the work is under an open content license such as Creative Commons.

Takedown policy

Please contact us and provide details if you believe this document breaches copyrights. We will remove access to the work immediately and investigate your claim.



Contents lists available at ScienceDirect

Progress in Nuclear Magnetic Resonance Spectroscopy

journal homepage: www.elsevier.com/locate/pnmrs

Relaxivity of manganese ferrite nanoparticles

Joop A. Peters

Biocatalysis, Department of Biotechnology, Van der Maasweg 9, 2629 HZ Delft, the Netherlands

Edited by David Gadian and David Neuhaus



ARTICLE INFO

Article history:

Received 10 July 2020

Accepted 26 July 2020

Available online 3 August 2020

Keywords:

MRI contrast agents

Magnetization

Transverse relaxivity

Longitudinal relaxivity

Zn-doping

ABSTRACT

Manganese ferrite nanoparticles are superparamagnetic and have very high saturation magnetization, which makes them candidates for application as MRI contrast agents. Because these nanoparticles are very effective enhancers of transverse relaxation, they are particularly suitable as negative (T_2 -weighted) contrast agents. The magnitude of the relaxivity of nanoparticulate Mn ferrites seems to be determined mainly by the method of preparation, their dimensions, and their saturation magnetization.

© 2020 The Author(s). Published by Elsevier B.V. This is an open access article under the CC BY license (<http://creativecommons.org/licenses/by/4.0/>).

Contents

1. Introduction	73
2. Relaxivity of superparamagnetic nanoparticles	73
2.1. The motional averaging regime (MAR)	74
2.2. The static dephasing regime (SDR)	75
2.3. The partial refocusing regime (PRR)	75
3. Relaxivity of manganese ferrite nanoparticles	76
3.1. Magnetization of manganese ferrite nanoparticles	76
3.2. Influence of the size of the nanoparticles	77
3.3. Influence of the preparation and the composition of the manganese ferrite	79
3.3.1. Stoichiometric manganese ferrites (MnFe_2O_4)	80
3.3.2. Non-stoichiometric manganese ferrites ($\text{Mn}_x\text{Fe}_{3-x}\text{O}_4$)	81
3.3.3. Manganese ferrites doped with zinc ($\text{Zn}_x\text{Mn}_{1-x}\text{Fe}_2\text{O}_4$)	82
3.4. Influence of the shape of the nanoparticles	84
3.5. Effects of coating and attachment of targeting vectors	84
3.6. Clustering of manganese ferrite nanoparticles	86
3.7. Manganese ferrites as T_1 MRI contrast agent	88
3.8. Manganese ferrites as dual T_1 - T_2 MRI contrast agent	89
4. Conclusions	89
Declaration of Competing Interest	90
Acknowledgment	90
Funding	90
References	90

E-mail address: J.A.Peters@tudelft.nl

<https://doi.org/10.1016/j.pnmrs.2020.07.002>

0079-6565/© 2020 The Author(s). Published by Elsevier B.V.

This is an open access article under the CC BY license (<http://creativecommons.org/licenses/by/4.0/>).

1. Introduction

Magnetic resonance imaging (MRI) is a powerful tool in medical diagnostics, producing images that reflect differences in intensities of ^1H NMR resonances, usually of water protons. These intensities are proportional to local ^1H concentrations and can be modulated by longitudinal ($R_1 = 1/T_1$) and transverse ($R_2 = 1/T_2$) relaxation rates, and by a number of other factors, including diffusion. In the initial paper reporting the invention of MRI, Lauterbur demonstrated that the contrast in images of phantoms can be altered by enhancement of the water ^1H relaxation rates by the addition of the paramagnetic MnSO_4 [1]. Later, paramagnetic contrast agents (CAs) based on other paramagnetic ions such as Gd^{3+} , Dy^{3+} , Ho^{3+} , and Fe^{3+} were introduced [2].

The efficacy of a relaxation rate enhancing CA is usually expressed by its relaxivity, the longitudinal or transverse relaxation rate enhancement normalized for a solution with a concentration of 1 mM of paramagnetic metal ions (r_1 and r_2 , respectively). MRI CAs can be distinguished according to the ratio r_2/r_1 . CAs that increase R_1 significantly more than R_2 give rise to bright areas in T_1 -weighted images and are called positive or T_1 CAs. T_2 or negative CAs increase R_2 of water protons significantly more than R_1 and produce dark areas in T_2 - or T_2^* -weighted images.

The CAs that are most frequently applied in clinical practice are positive Gd^{3+} -based agents. Free Gd^{3+} ions are toxic, and therefore their presence in vivo must be avoided. For the current clinical Gd^{3+} -based CAs, this is achieved by sequestering the metal ion using a strong chelating ligand, usually a DTPA- or DOTA-derivative [3–6].

Features of MRI include high spatial and temporal resolution, deep tissue penetration, and lack of ionizing radiation. However, the low sensitivity of the presently applied clinical MRI CAs is a serious shortcoming, particularly because most of these CAs distribute rather unselectively over the body. Nanoparticles (NPs) may be employed to overcome this by delivering a high payload of CA and thus creating high local concentrations in regions of interest such as tumors and arterial plaques. The local accumulation may be further enhanced by attachment of targeting vectors to the NPs and/or by exploiting the enhanced permeability and retention effect, the propensity of NPs to accumulate in tumors through the leaky neovasculature.

Gd^{3+} -based CAs have been in use for more than three decades and have proven to be generally extremely safe. Only 0.03% of all administrations (about 100 million worldwide) gave rise to serious adverse effects [7,8]. The high thermodynamic and kinetic stability of the Gd^{3+} -chelates are important safety factors; the half-life of the undissociated complex is large relative to the residence time in the body. However, reports of nephrogenic systemic fibrosis associated with linear Gd^{3+} -based MRI contrast agents (Gd^{3+} complexes of DTPA derivatives) in people with late-stage renal failure [8–10] and observations of long-term Gd^{3+} retention and accumulation in the brains of patients with normal renal function [11–15], have given rise to concerns regarding this class of compounds. Although macrocyclic CAs (DOTA derivatives) show higher kinetic stability than linear agents by multiple orders of magnitude, low levels of deposition of Gd^{3+} have been reported for these agents as well.

The concerns about Gd^{3+} -based CAs have sparked renewed interest in the use of Gd^{3+} -free CAs, such as Mn-based CAs, for example [6,16]. Both high spin d^5 Mn^{2+} and d^4 Mn^{3+} complexes are paramagnetic and have potential as MRI CAs. Due to the higher electronic symmetry of Mn^{2+} , the electronic relaxation rates of Mn^{2+} are usually considerably slower than those of Mn^{3+} , making the latter more favorable for optimal longitudinal relaxivities. Free Mn^{2+} is less toxic than Gd^{3+} and it plays an important role as a

cofactor in many enzymatic reactions, including the antioxidant enzyme superoxide dismutase, as well as enzymes involved in neurotransmitter synthesis and metabolism in the brain. Therefore, there is almost no risk associated with long-term accumulation. However, its normal concentration in organisms is very low, for instance, $0.3\text{--}1 \mu\text{g L}^{-1}$ in human blood [17]. Despite its important biological role, high concentrations of free Mn^{2+} are neurotoxic, and therefore Mn^{2+} needs to be sequestered for safe application as an intravenous CA in humans. Largely due to its lower charge, complexes are usually less stable than corresponding ones of Gd^{3+} . It is important to ensure that the dissociation of Mn-based CAs is minimized in order to avoid any adverse side effects such as neurotoxicity. On the other hand, given the inherently low sensitivity of MRI CAs, the increase in relaxation rate should be as high as possible. Finding a balance between kinetic stability and optimal sensitivity is an important challenge in the design of Mn-based CAs for human applications.

Superparamagnetic iron oxide nanoparticles (SPIOs) have found application in MRI as negative or T_2 CAs and ultrasmall iron particles (USPIOs) are used as positive or T_1 CAs [18]. During the last decade, manganese ferrites have attracted much attention, mainly because of their applications as T_2 CAs in highly sensitive MRI probes. NPs based on mixed Mn-Fe oxides are interesting in this respect because they can be tuned to optimize the r_2 to values that are higher than for iron oxides, whereas ultrasmall NPs usually have higher r_1 values thanks to the slower electronic relaxation rate of Mn as compared to that of Fe. Here, Mn-ferrite NPs with potential as MRI CA are reviewed with a focus on the relaxivity aspects at magnetic field strengths between 0.5 and 1.5 T, at which most clinic MRI scanners operate currently [19,20]. Mixed Mn-Zn ferrites are included in this review but other mixed ferrites such as those with Co and Ni are not because these materials may be cytotoxic [21–24] and thus not very attractive for application as MRI CA.

2. Relaxivity of superparamagnetic nanoparticles

Superparamagnetic NPs with sizes less than about 20 nm usually contain a single Weiss domain, which means that the electron spins in an NP are aligned to produce a large overall magnetic moment that is the sum of the magnetic moments of the magnetic atoms that compose that NP. A single molecule of MnFe_2O_4 has a magnetic moment of a few μ_B ($\mu_B = \text{Bohr magneton}$). But a spherical NP of MnFe_2O_4 with a diameter of 10 nm contains 6840 molecules and therefore has an overall magnetic moment that is a factor 6840 higher than that of a single molecule. The overall magnetization vector usually has two stable antiparallel orientations with respect to the crystallographic axes, which are denoted as the easy directions. Superparamagnetism is a regime where the correlation time of flipping of the overall magnetic moment is shorter than the experimental measuring time or in other words, the thermal energy of the system ($k_B T$) is greater than the energy barrier between easy directions of the overall magnetic moment. Consequently, the magnetization in the absence of a magnetic field is zero. The state at lower temperatures is called the blocked (ferromagnetic) state and the transition temperature between the two regimes is the blocking temperature (T_B). At high temperatures, the superparamagnetic regime is limited by the Curie temperature (T_C), where the thermal energy exceeds the energies of the antiferromagnetic coupling between two adjacent nearest metal cations (the superexchange). Above T_C , the system becomes paramagnetic.

Several theoretical models have been developed for the understanding of the proton relaxivities of aqueous suspensions of superparamagnetic iron oxide NPs [25], and they can also be applied for Mn-ferrites. These models generally provide a good qualitative description of structure-relaxivity relationships.

The proton relaxivity of superparamagnetic NPs in aqueous media has inner- and outer-sphere contributions. The inner-sphere contributions arise from water protons that exchange between metal atoms at the surface and the bulk and generally can be modeled by the Solomon-Bloembergen-Morgan equations in a way similar to Gd^{3+} and Mn^{2+} chelates [16,18,26]. Often the inner-sphere relaxivity is neglected because it is assumed to be small compared to the outer-sphere relaxivity. The latter is due to water protons diffusing along the particles, without being bound. The outer sphere contribution to the relaxivity is determined by two mechanisms: (1) the Brownian rotation of the NP and (2) the flip of the crystal magnetization vector from one easy direction of anisotropy to another (the Néel relaxation). The correlation times associated with these mechanisms are τ_B and τ_N , respectively. For a spherical particle, these correlation times are given by Eqs. (1) and (2), where η is the dynamic viscosity, K the anisotropy constant of the material, k_B the Boltzmann constant, T the absolute temperature, V the volume of the NP, and d its diameter.

$$\tau_B = \frac{\pi \eta d^3}{2k_B T} \quad (1)$$

$$\tau_N = \tau_0 e^{KV/k_B T} \quad (2)$$

Mn-ferrite NPs are predominantly used as T_2 CAs. Only the ultrasmall NPs have sufficiently large r_1/r_2 ratios at 0.5–1.5 T to be suitable for application as T_1 or dual T_1 - T_2 CAs. An important parameter governing both r_1 and r_2 of NPs is the magnetization, expressed as magnetic moment of the nanoparticle (m_{NP}) per unit volume (M) or per unit of mass (σ), respectively (see Eq. (3)). Here, ρ is the density. Since saturation of the magnetization of Mn-ferrites generally occurs below 0.5 T (see below), the magnetization considered here usually is the value at saturation (M_s or σ_s). It would be convenient to express the magnetization in an analogous manner to relaxivities, i.e. per mole magnetic metal. In the literature, however, σ -values are usually expressed per kg bare NPs, but a few authors express them per kg metal, per kg Fe, or per kg coated NPs. Unless stated otherwise, the σ -values in the present review are expressed in $A\ m^2\ kg^{-1}$ bare NP.

$$M = \frac{m_{NP}}{V} \quad (A\ m^{-1}) \quad \text{or} \quad \sigma = \frac{m_{NP}}{V\rho} \quad (A\ m^2\ kg^{-1}) \quad (3)$$

M is proportional to the Larmor frequency shift associated with the NP ($\Delta\omega$), which at the equator (defined relative to the B_0 -axis) on the surface of a spherical particle is given by Eq. (4), where γ_H is the gyromagnetic ratio of the 1H nucleus and μ_0 the permeability of a vacuum.

$$\Delta\omega = \frac{\gamma_H \mu_0 M}{3} = \frac{\gamma_H \mu_0 \rho \sigma}{3} \quad (4)$$

Recently, Vuong et al. have reviewed studies on the modeling of outer-sphere relaxation rates induced by superparamagnetic NPs [25]. Relaxation rates as a function of the 1H Larmor frequency (LF), i.e. nuclear magnetic dispersion (NMRD) profiles, have been described with models for the motional averaging regime (MAR), which is defined by the condition $\Delta\omega\tau_D < 1$ ($\tau_D = d^2/4D$, where τ_D is the diffusion correlation time and D the water diffusion coefficient). The longitudinal relaxation can then be described by Eq. (5) [27], where C_{NP} is the number of particles per m^3 , $L(x)$ is the Langevin function ($L(x) = \coth x - x^{-1}$) with $x = m_{NP}H/k_B T$.

$$R_1 = \frac{8\pi}{135} \left(\frac{\mu_0}{4\pi}\right)^2 m_{NP}^2 \gamma_H^2 \frac{C_{NP}}{dD} \mathcal{R} \quad (5)$$

For low anisotropy energy, the Néel relaxation dominates ($\tau_N \ll \tau_B$), \mathcal{R} is given by Eqs. (6)–(8), P is an empirical function depending on the anisotropy energy, and J_F and J_A are the Freed and Ayant spectral densities, respectively [27].

$$\begin{aligned} \mathcal{R} = & 14P \frac{L(x)}{x} J_F(\omega_S, \tau_D, \tau_N) \\ & + \left[14(1-P) \frac{L(x)}{x} + 6 \left(1 - 2 \frac{L(x)}{x} - L^2(x) \right) J_F(\omega_H, \tau_D, \tau_N) \right] \\ & + 6L^2(x) J_A(\omega_H, \tau_D) \end{aligned} \quad (6)$$

$$J_F(\omega, \tau_D, \tau_N) = \text{Re} \left(\frac{1 + (1/4)z^{1/2}}{1 + z^{1/2} + (4/9)z + (1/9)z^{1/2}} \right) \quad \text{with } z = \frac{\tau_D}{\tau_N} + \omega\tau_D i \quad (7)$$

$$J_A(\omega, \tau_D) = \frac{1 + (5/8)z + (1/8)z^2}{1 + z + (1/2)z^2 + (1/6)z^3 + (4/81)z^4 + (1/81)z^5 + (1/648)z^6} \times \text{with } z = (2\omega\tau_D)^{1/2} \quad (8)$$

When the anisotropy energy is so high that the magnetic moment of the particle is fixed on its anisotropy axis, the Brownian relaxation dominates the Néel relaxation and then, according to the rigid dipole model, \mathcal{R} is given by Eqs. (7)–(10) [28].

$$\begin{aligned} \mathcal{R} = & \left[14 \frac{L(x)}{x} J_F(\omega_H, \tau_D, \tau_{\perp}) + 6L^2(x) J_A(\omega, \tau_D) \right. \\ & \left. + 6 \left(1 - \frac{2L(x)}{x} - L^2(x) \right) J_F(\omega_H, \tau_D, \tau_{\parallel}) \right] \end{aligned} \quad (9)$$

$$\tau_{\perp} = \frac{2L(x)}{x - L(x)} \tau_B \quad (10)$$

$$\tau_{\parallel} = \frac{x}{L(x)} \left(\frac{1}{x^2} - \frac{1}{\sinh^2 x} \right) \tau_B \quad (11)$$

Simulations with the above models typically give 1H NMRD profiles as shown in Fig. 1. These profiles show that the highest r_1 values in the range of the currently most used clinical MRI scanners (0.5–1.5 T or $LF = 20$ –64 MHz) can be reached with small NPs ($d \leq 10$ nm) that have high magnetization.

The transverse relaxation is ascribed to the magnetic field inhomogeneities created by the superparamagnetic NPs, which leads to loss of phase coherence of the precessing nuclear spins. Various models have been developed to describe the resulting enhancement of transverse relaxation rates of spherical superparamagnetic NPs [18,25,29–32]. Three regimes can be distinguished with limits defined by the diffusion correlation time (τ_D), the static correlation time ($\Delta\omega^{-1}$), and the correlation time τ_{CP} (half the time interval between successive 180° pulses in a Carr-Purcell-Meiboom-Gill (CPMG) pulse sequence).

2.1. The motional averaging regime (MAR)

This regime is also called the outer-sphere regime and can be applied for small particles if $\tau_D \Delta\omega < 1$. Under this condition, protons experience a large range of magnetic fields during their diffusion along the NPs. This results in a motional averaging effect of these NPs. For high magnetic field strengths (>1 T), the transverse relaxation rate can then be described by Eq. (12) [32,33].

$$R_2 = R_2^* = \frac{16}{45} f \tau_D (\Delta\omega)^2 \quad (12)$$

Here R_2 and R_2^* are the transverse relaxation rates measured in the presence and absence of refocusing pulses, respectively, and f is the volume fraction of the NPs. Since the relaxation rate is proportional to $(\Delta\omega)^2$, it is also proportional to M^2 (or σ^2 , see Eq. (4)), which is, for Mn-ferrites at magnetic field strengths larger than 1 T, usually at the saturation value (M_s^2 or σ_s^2) or somewhat higher due to a paramagnetic contribution to the magnetization (see Section 3.2).

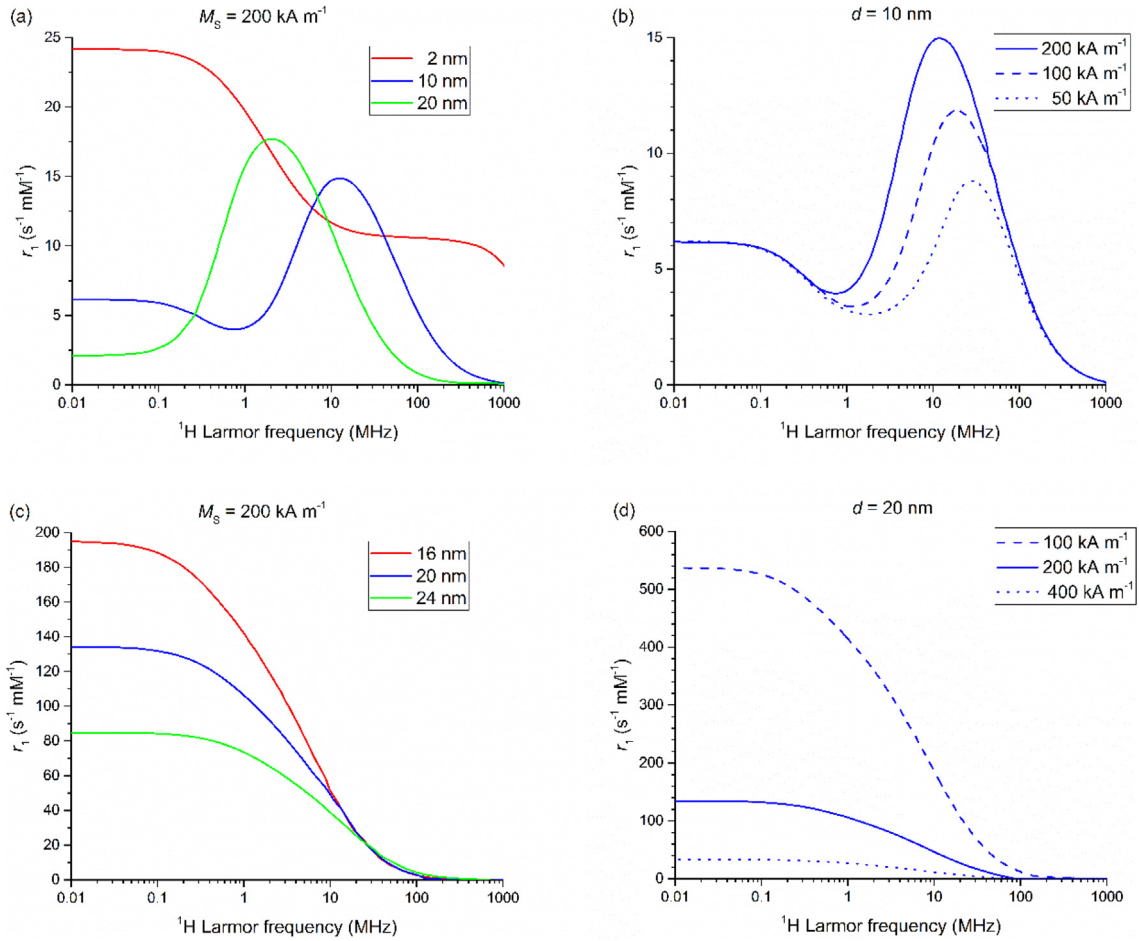


Fig. 1. Simulated ^1H NMRD profiles using the low anisotropy (top row) and the high anisotropy model (bottom row) for various M_s and d values. The values for the other parameters were: $D = 3 \times 10^{-9} \text{ m}^2 \text{ s}^{-1}$, $T = 310 \text{ K}$, $P = 0.8$, $\eta = 0.6915 \text{ Pa s}$, $\tau_N = 10^{-9} \text{ s}$. Adapted from [25].

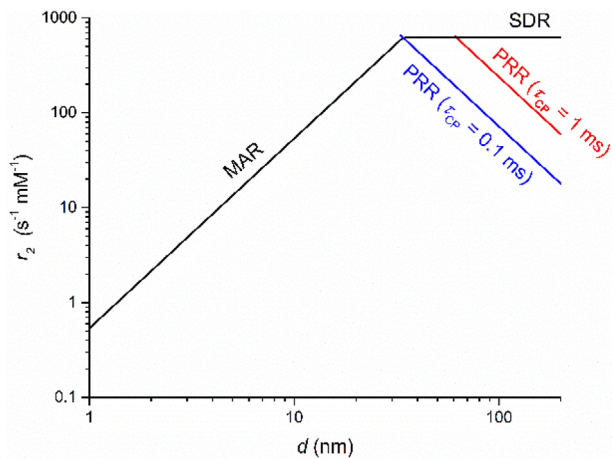


Fig. 2. The dependence of the transverse relaxivity on the diameters of spherical Mn-ferrite NPs for the MAR, SDR, and PRR as predicted with Eqs. (12), (13), and (15), respectively, assuming $D = 3 \times 10^{-9} \text{ m}^2 \text{ s}^{-1}$, $\sigma_s = 60 \text{ A m}^2 \text{ kg}^{-1}$, $f = 1.58 \times 10^{-5}$ (corresponding to a concentration of 1 mM paramagnetic ions). The red line is calculated for $\tau_{CP} = 1 \text{ ms}$ and the blue one for $\tau_{CP} = 0.1 \text{ ms}$. In the MAR and the SDR as long as the PRR is not reached, $r_2 = r_2^*$. In the PRR, $r_2 < r_2^*$.

2.2. The static dephasing regime (SDR).

For relatively large NPs, when $\tau_D \Delta\omega > 2.72$, the diffusion can be practically neglected and R_2^* is solely dependent on $\Delta\omega$. Its magnitude can then be approximated by [34,35]:

$$R_2^* = \frac{2\pi}{3\sqrt{3}} f \Delta\omega \quad (13)$$

Eq. (13) is also a good approximation for R_2 as long $\tau_D < \tau_L$ [36,37], where τ_L is given by:

$$\tau_L = \frac{1.49}{\Delta\omega} x^{1/3} (1.52 + fx)^{5/3} \quad (14)$$

with $x = \Delta\omega \tau_{CP}$. In the SDR regime, r_2 is linearly proportional to M .

2.3. The partial refocusing regime (PRR).

When $\tau_D > \tau_L$, the refocusing of the transverse magnetization during the CPMG pulse sequence becomes inefficient, which results in a decrease in R_2 compared to R_2^* to an extent that depends on the magnitude of τ_{CP} according to Eq. (15) [18,36,37].

$$R_2 = \frac{1.8fx^{1/3}(1.52 + fx)^{5/3}}{\tau_D} \quad (15)$$

It can be concluded that upon an increase of the size of NPs, R_2^* increases linearly with τ_D until the SDR is reached, where after R_2^* as a function of τ_D is constant. In the MAR, R_2 and R_2^* are equal, whereas, in the PRR, R_2 becomes smaller than R_2^* if $\tau_D > \tau_L$ (see Fig. 2). Therefore, maximum relaxivities will occur for NPs with diameters that correspond to the transition between MAR and SDR. The region with maximum R_2 moves to smaller diameters upon an increase of σ_s . A gap between R_2 and R_2^* and dependence of R_2 on τ_{CP} are indications that the sample is in the PRR.

Although sharp transitions between the regimes shown in Fig. 2 are not realistic, this model reasonably describes the relaxation behavior of Mn-ferrite NPs, at least qualitatively. A more elaborate model has been described, that predicts a smooth cross-over between the MAR and the SDR regimes [25,38].

Coating a bare superparamagnetic NP with a diamagnetic substance naturally has consequences for its relaxivity. Taking into account the distance dependence of $\Delta\omega$, f , and τ_D , the following scaling may be applied for spherical NPs coated with a water-impermeable layer:

$$\Delta\omega_{imp} = \Delta\omega_{core} \left(\frac{d_{core}}{d_{imp}} \right)^3 \quad (16)$$

$$f_{imp} = f_{core} \left(\frac{d_{imp}}{d_{core}} \right)^3 \quad (17)$$

$$\tau_{D,imp} = \tau_{D,core} \left(\frac{d_{imp}}{d_{core}} \right)^2 \quad (18)$$

Here, the subscripts imp and core denote the parameters for the coated and the bare NP, respectively. Substituting Eqs (16)–(18) into Eqs. (12), (13), and (15) gives the effect on R_2 and R_2^* of coating with an impermeable layer [39].

$$\text{MAR: } R_{2,imp} = R_{2,imp}^* = R_{2,core} \left(\frac{d_{core}}{d_{imp}} \right) \quad (19)$$

$$\text{SDR: } R_{2,imp}^* = R_{2,core}^* \quad (20)$$

$$\text{PRR: } R_{2,imp} = R_{2,core} \quad (21)$$

This shows that an impermeable coating decreases the transverse relaxivity in the MAR, but does not affect it outside this regime. Eqs. (16) and (18) show that the product $\tau_D\Delta\omega$ will decrease upon coating of an NP. Consequently, NPs that are in the MAR will remain in that region upon coating. Similarly, it can be demonstrated that this is not necessarily the case for the SDR.

For water-permeable coatings, the situation is more complicated; the value of f cannot be calculated directly from the diameters before and after coating and the self-diffusion into the pores may be slower than in the bulk water, which may increase the local τ_D [40]. The latter effect will, by contrast, lead to an increase in r_2 in the MAR, no r_2 -effect in the SDR, and a decrease in r_2 in the PRR upon such coating. Monte Carlo simulations have shown that, also in the region of transition between MAR and SDR, decreased R_2^* values are obtained [41]. Furthermore, protons exchanging between locations close to the paramagnetic centers and the bulk might contribute to the relaxivity of these systems. It should be noted that coating, particularly when it involves coordination of paramagnetic metal ions on the surface of the core, may influence the value of σ_s as well (see Section 3.5).

3. Relaxivity of manganese ferrite nanoparticles

3.1. Magnetization of manganese ferrite nanoparticles

Nanoparticulate assemblies of single domain manganese ferrites exhibit superparamagnetic behavior. A typical curve of the magnetization σ against the magnetic field strength H at room temperature is fully reversible without magnetic coercivity and remanence (see for example Fig. 3) [42]. The latter is essential for biomedical applications because coagulation due to residual magnetization outside of a magnetic field is undesirable. Saturation of the magnetization for NPs with diameters larger than 5 nm generally occurs below 0.5 T at values that are higher than

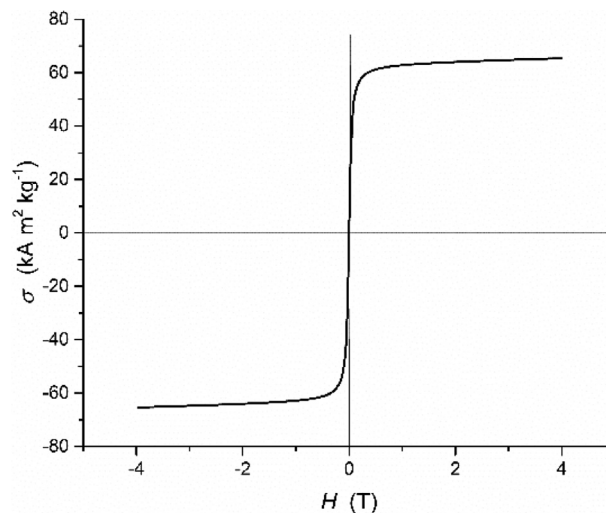


Fig. 3. A σ – H curve of $[\text{Mn}_{0.78}\text{Fe}_{0.22}](\text{Mn}_{0.22}\text{Fe}_{1.78})\text{O}_4$ NPs. Adapted from Ref. [42].

for Fe_3O_4 nano-assemblies. The curve of the magnetization as a function of the magnetic field strength H can be described by a Langevin function (22), where m_{NP} is the magnetic moment of a single particle. Fitting of the experimental σ – H curve with this equation affords the saturation magnetization σ_s (in $\text{A m}^2 \text{kg}^{-1}$, often expressed as emu g^{-1}) and m_{NP} . The ratio σ_s/m_{NP} is equal to the number of particles per kg (N) and $m_{\text{NP}} = n\mu_{\text{mol}}$, where n is the number of molecules (formula units) per NP and μ_{mol} is the magnetic moment per molecule ferrite [43].

$$\begin{aligned} \sigma &= \sigma_s \left[\coth x - \frac{1}{x} \right] = Nm_{\text{NP}} \left[\coth x - \frac{1}{x} \right] \quad \text{with } x = \frac{m_{\text{NP}}H}{k_B T} \\ &= \frac{n\mu_{\text{mol}}H}{k_B T} \end{aligned} \quad (22)$$

NPs with high σ_s values are favorable for application as T_2 CAs as well as for efficient heat generation in AC magnetic field hyperthermia therapy of cancer and other diseases [44]. The generation of heat has also been exploited to induce drug release from capsules with a thermolabile shell loaded with MnFe_2O_4 NPs and the anti-cancer medicine doxorubicin [45]. Therefore, it is important to design nanoparticles with high and tunable σ_s values. The main parameters that can be tuned to optimize the relaxivity are the composition of the ferrite, the size of the NPs, their shape, and their coating.

Spinel ferrites are ceramic ferrimagnetic iron oxide compounds with a complex crystal structure in which oxygen anions are in a face-centered cubic arrangement (space group $Fd3m$), while the much smaller intervening 2- and 3-valent metal cations occupy two different sublattices, denoted by A (or T_d) and B (or O_h). In the unit cell, the metal ions are coordinated by oxygen atoms, 8 of the 64 A-sites tetrahedrally and 16 of the 32 B-sites octahedrally whereas the remaining sites are not occupied (see Fig. 4) [46,47]. The general formula of these spinels can be represented as $[\text{M}_i^{2+}{}_{1-i}\text{Fe}_i^{3+}]^{\text{A}}(\text{M}_i^{2+}\text{Fe}_{2-i}^{3+})^{\text{B}}\text{O}_4$, where M is a metal, usually a transition metal or Mg. The superscripts A and B indicate the location of the metal ions and square and round brackets are used for the A- and B-sites, respectively. Two limiting arrangements can be discriminated: (1) structures with 8 M^{2+} ions at A-sites and 16 Fe^{3+} ions at B-sites ($i = 0$) are called normal spinels and (2) structures having 8 Fe^{3+} ions at the A-sites and B-sites occupied with both 8 Fe^{3+} - and 8 M^{2+} -ions ($i = 1$) are denoted as inverse spinels. In the above molecular formula, i is the fraction of M^{2+} ions at B-sites and is called the degree of inversion [48]. The thermodynamically most stable distribution of

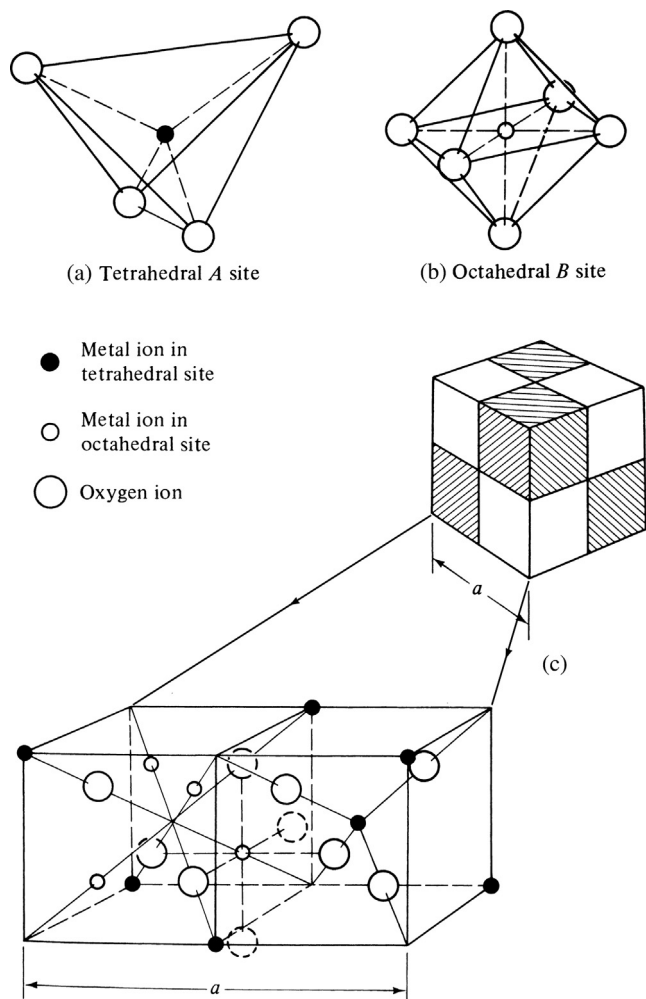


Fig 4. Structure of the unit cell of a cubic spinel. The four shaded octants are mutually identical, as are the unshaded octants. Reproduced from Ref. [46] with permission. Copyright 2008, John Wiley & Sons, Inc.

metal ions over the A- and B-sites depends on many factors including (1) the ion size: the smaller cations generally have a preference for tetrahedral A-sites, (2) the electronic configuration of the metal ions involved and their crystal field stabilization, (3) the Coulomb energy of the charged ions in the spinel lattice [47,49,50]. The normal spinel is the thermodynamically most stable Mn-ferrite, whereas most other ferrites of divalent ions show a preference for inverse spinel structures [47,51].

To a first approximation, insight into the saturation magnetization (σ_s) of spinel ferrites can be obtained by considering the spin only magnetic moments of the A- and B-sites at 0 K. Oxygen anion mediated exchange interactions between spins of neighboring metal ions determine the sign and the magnitude of σ_s . The AB, AA, and BB superexchange interactions tend to be negative, but all spin moments cannot be negative simultaneously [46]. Since the AB spin-interaction is usually the strongest, all A spin moments are parallel to one another and antiparallel to the B moments. A ^{57}Fe NMR study on Mn ferrites has demonstrated that in the presence of an external magnetic field, the B moments align in the direction of the field and the A moments in the opposite direction [52]. Mn^{2+} and Fe^{3+} both have 5 unpaired *d*-electrons and thus have a spin-only magnetic moment (μ) of $5 \mu_B$, whereas Fe^{2+} and Mn^{3+} have 4 unpaired *d*-electrons and thus both have $\mu = 4 \mu_B$ at 0 K. The net magnetic moment per formula unit of a ferrite (μ_{mol}) can be estimated by subtracting the summed magnetic moments

of the A sublattice from those of the B sublattice. In this way, it can be estimated that for the series of inverse spinel structures of MFe_2O_4 ($M = \text{Mn}^{2+}, \text{Fe}^{2+}, \text{Co}^{2+}, \text{Ni}^{2+}, \text{Cu}^{2+}, \text{Zn}^{2+}$), μ_{mol} at 0 K decreases with the number of unpaired *d*-electrons from 5 to 0 μ_B [53]. Moreover, the net magnetic moment of these metal ferrites ($M \neq \text{Mn}^{2+}$), is dependent on the degree of inversion.

It should be noted that the values of σ_s are maximal at 0 K and decrease to 0 at the Curie temperature (T_C), where the materials become paramagnetic (see for example Fig. 5). The shape of a curve of σ_s as a function of the temperature is the resultant of the curves for the sublattices A and B, which sometimes may lead to a non-continuous shape [46]. Furthermore, the values of many magnetic properties of NPs are not the same as those of bulk materials. For example, the Curie temperature of MnFe_2O_4 tends to increase whereas σ_s generally decreases with decreasing particle size (see Section 3.2) [46,47,54,55]. The value of T_C is dependent on the strength of the superexchange interaction between the A and the B sublattices and therefore on the cation distribution over these sites. An increase in *i* corresponds with the replacement of the Mn^{2+} - Fe^{3+} AB-superexchange interaction by the stronger Fe^{3+} - Fe^{3+} interaction leading to a rise of T_C .

For the MAR (see Section 2.1), r_2 is proportional to σ_s^2 and if it is assumed that the members of the MFe_2O_4 series (*M* is a transition metal ion) have about the same density, it follows that r_2 is approximately proportional to the square of the number of unpaired electrons of the metal ion *M*. Fig. 6 shows that this is in reasonable agreement with the experimental r_2 data. The high relaxivity of MnFe_2O_4 NPs has been exploited in tests of targeted probes based on these NPs demonstrating the potential in the detection of various types of diseases and in cell tracking [53,56–58].

3.2. Influence of the size of the nanoparticles

The size of NPs may influence the magnitudes of σ_s and τ_D , which are both parameters governing the transverse relaxivity (see Section 2). Often, the σ_s values of NPs are lower than predicted by estimation from the magnetic moments of the metal ions inside each particle. Moreover, an inspection of published σ -*H* curves shows that these curves sometimes continue to increase linearly with the magnetic field strength after “saturation”, particularly for the smallest NPs. This suggests that there is a paramagnetic contribution to the magnetization in addition to the superparamagnetic one. Therefore, a better fit can be obtained by including a term in Eq. (22) to account for this paramagnetic contribution

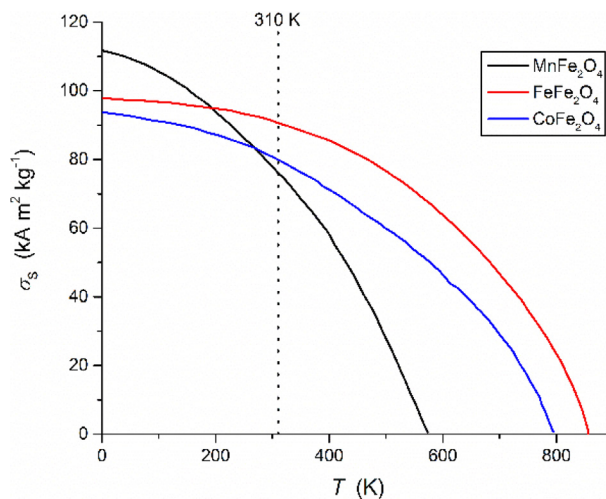


Fig. 5. The temperature dependence of σ_s of some bulk ferrites. Data from ref. [47].

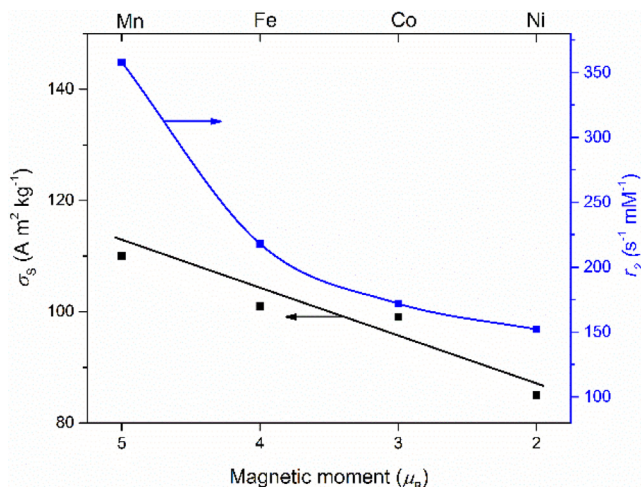


Fig. 6. σ_s at RT and τ_2 at 1.5 T and RT as a function of magnetic moments of the metal ion M in 12 nm NPs of $M\text{Fe}_2\text{O}_4$ spinels. Constructed with data from Ref. [53]. It should be noted that in Ref. [53] σ_s is expressed per mass of magnetic atoms, whereas other data in the present paper are expressed per mass of ferrite (formula weight) unless stated otherwise. The lines are intended only as guides to the eye.

(see Eq. (23)). A similar approach has been followed by Bulte et al. to fit the magnetization curves of iron oxide NPs [59]. Fitting of σ - H curves with Eq. (23) provides m_{NP} , σ_s , and C_{para} . If the paramagnetic contribution is negligible, division of σ_s by m_{NP} gives the number of superparamagnetic molecules (N) and thus also the weight or the volume of one NP can be calculated if the molecular weight and the density of the ferrite, n and μ_{mol} are known.

$$\sigma = \sigma_s \left[\coth x - \frac{1}{x} \right] + C_{\text{para}} H \quad \text{with} \quad x = \frac{m_{\text{NP}} H}{kT} = \frac{n \mu_{\text{mol}} H}{kT} \quad (23)$$

The paramagnetic contribution may be due to surface anisotropy effects due to atomic disorder and symmetry breaking. These effects result in orientations of surface spins that are not parallel with those of the core (this effect is also known as spin-canting). Canting of the surface spins in random directions results in a surface layer with net zero magnetization: a magnetically dead layer [60–62]. Possibly, the local Curie temperature in a paramagnetic layer is lower than that in a magnetically dead layer. The reduction in σ_s due to a dead layer can be related to its thickness (D_L) by Eq. (24), where d is the diameter of the NP. Simulations of σ as a function of d show that even a thin dead layer results in a large decrease in the value of σ_s of NPs with small diameters because the volume of the magnetically dead layer increases relative to that of the total volume of the NP (see Fig. 7).

$$\sigma_s = \sigma_s^{\text{bulk}} \left(\frac{d - 2D_L}{d} \right)^3 \quad (24)$$

Alternative Eq. (25) has been used in various publications to estimate the effect of a dead layer on the magnitude of σ_s [61,63–66].

$$\sigma_s = \sigma_s^{\text{bulk}} \left(1 - \frac{6D_L}{d} \right) \quad (25)$$

Since the magnetic moments of Mn^{2+} and Fe^{3+} are both $5 \mu_B$, the net magnetic moments of the normal and the inverse structures are identical ($5 \mu_B$ at 0 K). Therefore, it may be expected that at a given temperature, MnFe_2O_4 NPs always have the same σ_s . However, the experimental σ_s values are found to be in the range of 2–90 $\text{A m}^2 \text{kg}^{-1}$. In Fig. 8, values of σ_s obtained by fitting of 41 different published σ - H curves on spherical MnFe_2O_4 NPs [64,67–86] with Eq. (23) are displayed as a function of the reported diameters

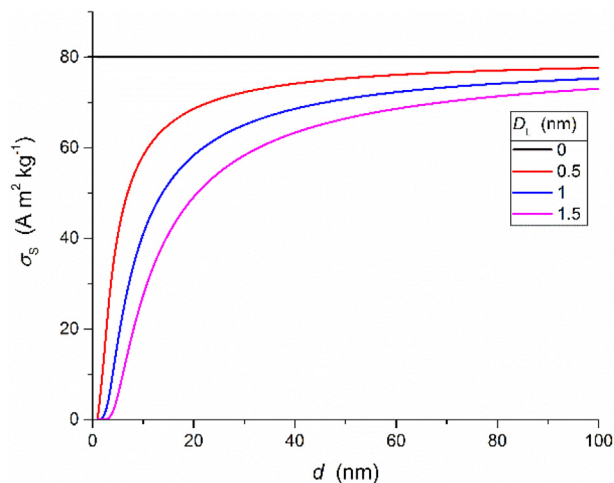


Fig. 7. Simulations with Eq. (24) of the effect of a dead layer on the value of σ_s . The value of σ_s is assumed to be $80 \text{ A m}^2 \text{kg}^{-1}$.

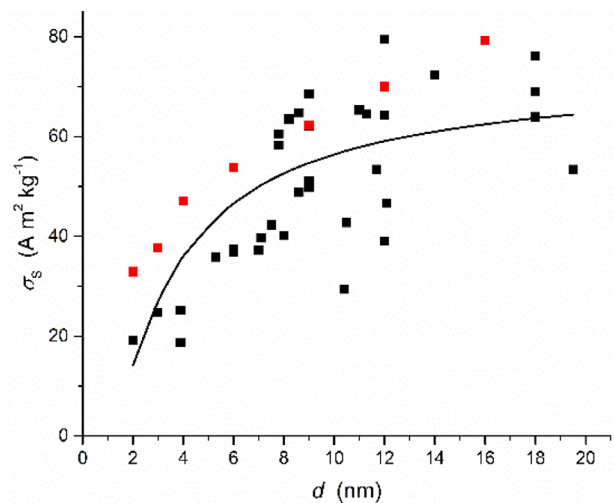


Fig. 8. Plot of σ_s versus d . The σ_s values have been obtained by fitting of reported σ - H curves with Eq. (23). The curve is calculated with the best-fit parameters of all σ_s data (black and red squares) with Eq. (24) (see text). Here, red squares are data of a set of NPs prepared using the same synthetic method (see text) [78].

(d) determined by transmission electron microscopy (TEM). Although the data points are rather scattered, they show a clear increasing trend in σ_s with d . Fitting of these data with Eq. (24) gives as best-fit parameters $\sigma_s^{\text{bulk}} = 74 \text{ A m}^2 \text{kg}^{-1}$ and $D_L = 0.4 \text{ nm}$. Considering the large extent of scattering in Fig. 8, the value for σ_s^{bulk} is in reasonable agreement with that measured in bulk material ($80 \text{ A m}^2 \text{kg}^{-1}$) [47]. A comparison of the best-fit value for D_L with the cell dimensions of the unit cell of MnFe_2O_4 (0.85 nm) suggests that the dead layer is formed mainly by the outer surface layer. This layer probably contains metal ions that are not fully coordinated, which may give rise to spin disorder. If in Fig. 8 only the data of NPs prepared using one particular procedure are considered, a better fit is obtained. For example, the red squares in Fig. 8, represent data for a series of MnFe_2O_4 NPs that were prepared by thermolysis of metal salts in the presence of oleylamine (OA). The latter had a threefold role: it served as a solvent, as a reducing agent and as a capping agent. The resulting NPs showed σ_s values (at 300 K) increasing with the particle size

from about 33 to 80 A m² kg⁻¹ (after correction for the weight of the oleylamine at the surface).[78] The application of the fitting procedure described above gives $\sigma_s^{\text{bulk}} = 81 \text{ A m}^2 \text{ kg}^{-1}$ and $D_L = 0.3\text{-nm}$ as best-fit parameters.

The influence of the NP diameter on the transverse relaxivity through τ_D is dependent on the operative regime. From Fig. 2, it may be concluded that for a particular σ_s value, maximum transverse relaxivities may be expected in the SDR between τ_{SDR} and τ_L . Fig. 9 displays a plot of σ_s versus d in which the borders between the SDR and the MAR and PPR are represented by lines simulated with $\tau_D = 2.72/\Delta\omega$ and $\tau_D = \tau_L$, respectively. Since under the SDR regime, r_2 is linearly proportional to $\Delta\omega$ and thus also to σ_s (see Eqs. (3) and (4)), the highest transverse relaxivities will be found for the highest σ_s values in the SDR in Figs. 2 and 9. Almost all single-crystalline Mn-ferrite superparamagnetic NPs have core diameters below 20 nm and the maximum σ_s reported is for Zn_{0.4}Mn_{0.6}Fe₂O₄ (175 A m² kg⁻¹ magnetic atom $\approx 107 \text{ A m}^2 \text{ kg}^{-1}$ material). Accordingly, very high r_2 values (860 s⁻¹ mM⁻¹, see Section 3.3.3) have been reported for this system [87]. As can be seen in Fig. 9, the relaxivity is near the boundary of the MAR and the SDR and thus is approximately the highest possible r_2 within this class of CAs. Increasing the diameter by coating with a water-impermeable diamagnetic layer is counter-effective since the beneficial effect of the increase in τ_D is less than the detrimental effect of the decrease of σ_s of the NP. However, clustering of NPs by encapsulation or by inclusion in more bulky structures may bring the system under study into the SDR. If a very high r_2 is required, very large sizes are unfavorable, because then the PRR may be reached, where r_2 becomes smaller than in the SDR. However, it should be noted that r_2^* is independent of the NP size in both SDR and PRR.

The size of NPs is not only important with regard to the relaxivity but it also determines to a great extent their biodistribution. Generally, small particles (20–30 nm) are eliminated by renal excretion, while particles 30–150 nm are taken up by the reticuloendothelial system of the liver and other organs [88]. For optimal cell binding of NPs, their size should be <50 nm [89]. It should be noted that other parameters including shape and zeta potential also play important roles in biodistribution and pharmacokinetics. Globally, it can be stated that small particles (<30 nm) have the largest chance to reach their target.

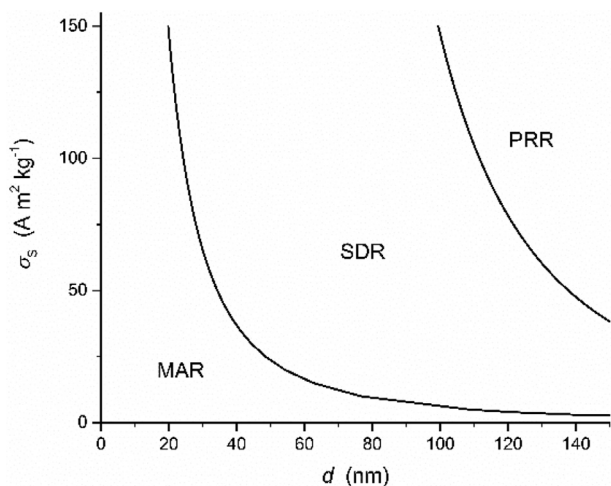


Fig. 9. Schematic representation of the MAR, SDR, and PRR regimes. The lower curve represents the σ_s , and d values for which $\tau_D \Delta\omega = 2.72$, whereas at the upper curve $\tau_D = \tau_L$. See Eq. (14). These curves are calculated assuming that the concentration Fe + Mn atoms = 1 mM, $\rho = 4.96 \text{ kg L}^{-1}$, $D = 3 \times 10^{-9} \text{ m}^2 \text{ s}^{-1}$, and $\tau_{\text{CP}} = 0.1 \text{ ms}$.

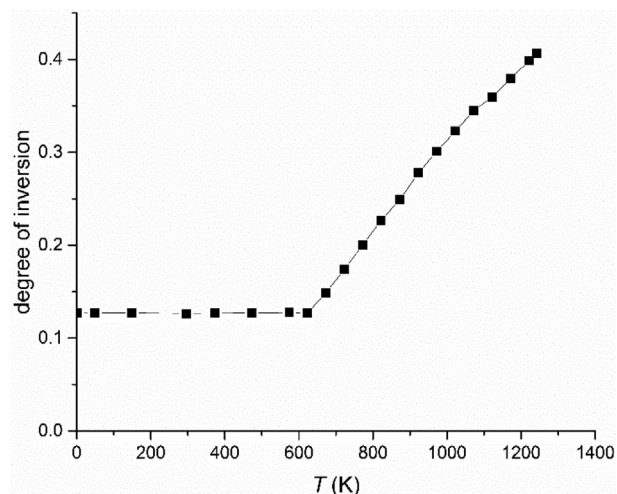


Fig. 10. Degree of inversion of MnFe₂O₄ as a function of the temperature. Adapted from ref. [96].

On the other hand, larger particles have higher σ_s and thus higher r_2 because of the reduced spin-canting effect. By compromising on these opposite requirements, Lee et al. have prepared 16 nm Mn-doped ferrite NPs (ratio Fe/Mn ≈ 4) coated with 2,3-dimercaptosuccinic acid (DMSA) having $\sigma_s = 124.3 \text{ A m}^2 \text{ kg}^{-1}$ metal and $r_2 = 420 \text{ s}^{-1} \text{ mM}^{-1}$ at 40 °C [90]. After conjugating monoclonal antibodies against specific cancers to these NPs, it was possible to detect as few as 2 cancer cells in 1 μL sample volumes of unprocessed fine-needle aspirates of tumors and to profile the expression of several cellular markers in less than 15 min with the aid of a specially developed highly sensitive micro NMR probe.

3.3. Influence of the preparation and the composition of the manganese ferrite

Mn-ferrite NPs can be prepared by several methods [50,91–94], the most common of which include (1) calcination of mixtures of the appropriate metal oxides at temperatures above 1200 °C and subsequent ball milling, (2) hydrothermal or solvothermal coprecipitation of Mn- and Fe-compounds, eventually followed by heat treatment, and (3) solvothermal decomposition of metal complexes, often acetylacetonates in the presence of a surfactant such as oleic acid and/or oleylamine. Usually, the particle size is then controlled with a seed-growth procedure [93]. NPs with hydrophobic coatings have to be made hydrophilic by ligand exchange.

The degree of inversion, i , can be influenced by the preparation method and particularly by the thermal treatment. Accordingly, the magnetic properties also, including σ_s , the magnetic anisotropy, the blocking temperature, and the Curie temperature are dependent on the preparation and temperature treatment [42]. During the co-precipitation method, higher growth rates appeared to result in higher disorder in the cation distribution and thus in higher i -values and consequently also in higher Curie temperatures [95].

Neutron powder diffraction (NPD) studies have shown that the dependency of the degree of inversion of the Mn-ferrites on the heat treatment during their preparation can be ascribed to structural changes due to cation partitioning between the A- and B-sites (for example, $[\text{Mn}^{2+}]^{\text{A}} + [\text{Fe}^{3+}]^{\text{B}} \rightleftharpoons [\text{Mn}^{2+}]^{\text{B}} + [\text{Fe}^{3+}]^{\text{A}}$), which begins between 573 K and 623 K [96–98]. Between 623 K and 1247 K, the value of i of MnFe₂O₄ increased monotonically from 0.13 to 0.41 (see Fig. 10) [96]. Quenching by fast cooling from temperatures above 870 K affords a metastable state with $i \approx 0.22$, which indicates that i follows its equilibrium value down to about

870 K where it freezes [97]. At lower temperatures, the equilibration of the cation distribution becomes extremely slow.

A complicating factor in studies of Mn-ferrites may be the occurrence of the redox equilibrium between Mn^{2+} and Fe^{3+} ($\text{Mn}^{2+} + \text{Fe}^{3+} \rightleftharpoons \text{Mn}^{3+} + \text{Fe}^{2+}$) and (partial) oxidation of Mn^{2+} to Mn^{3+} by air. The latter may already occur during the synthesis, for example by co-precipitation, particularly under highly basic conditions [99]. Oxidation can be prevented by working in a strictly inert atmosphere, particularly during hydrolytic procedures at high pH. An elegant way to remove traces of Mn^{3+} in ferrites is by reduction into Mn^{2+} with hydrogen peroxide in an acidic medium ($2\text{Mn}^{3+} + \text{H}_2\text{O}_2 \rightarrow 2\text{Mn}^{2+} + \text{O}_2 + 2\text{H}^+$) [100,101]. A hydrothermal synthesis of $\text{Mn}_{0.62}\text{Zn}_{0.41}\text{Fe}_{1.97}\text{O}_4$ carried out under less strictly inert conditions has been reported to result in contamination with 1% $\alpha\text{-Fe}_2\text{O}_3$ and 2% $\text{Mn}_{3-x}\text{Zn}_x\text{O}_4$ [102].

Because Mn^{3+} -ions prefer a location in the B-site thanks to a relatively high crystal-field stabilization, oxidation also affects i . Since, after oxidation, the magnetic moment of Mn is no longer the same as that of Fe^{3+} but decreases from 5 to 4 μ_B , the σ_S -value is influenced by changes in both the degree of oxidation and the degree of inversion.

For a full understanding of the magnetic properties of spinel Mn-ferrites knowledge of the stoichiometry, the valence of the metal ions, and their distribution over the A- and B-sites is indispensable, requiring measurements that are challenging [103]. Unfortunately, many publications lack complete information in this respect. The molar ratio Mn:Fe can be determined by inductively coupled plasma optical emission spectroscopy (ICP-OES) or by X-ray powder diffraction (XRD), and NPD can afford cation distribution data. The latter technique may also provide the magnetic moments of the A- and B-sites. ^{57}Fe Mössbauer spectra have been used to obtain information on valences of the Fe -cations and their distribution, but it cannot always be used to determine the location of Fe^{3+} -ions [98]. X-ray absorption fine structure (XAFS), X-ray absorption near edge structure (XANES), electron energy loss spectroscopy (EELS), X-ray photoelectron spectroscopy (XPS), and low-temperature spin-echo ^{55}Mn - and ^{57}Fe -NMR studies have been applied to determine the valences of metal ions in Mn-ferrites [52,67,104,105].

The thickness of a dead layer on the NP is also dependent on the preparation procedure. For example, the preparation of MnFe_2O_4 NPs by co-precipitation of MnCl_2 and FeCl_3 in aqueous NaOH has been reported to produce NPs with a thicker dead layer than by precipitation with aqueous solutions of alkanolamines. A similar phenomenon was observed with MnFe_2O_4 NPs prepared by solvothermal procedures using oleylamine as both the solvent and the capping agent [78]. These effects were attributed to the coordination of metal ions by the amines, which provides a higher surface spin order [60,78].

3.3.1. Stoichiometric manganese ferrites (MnFe_2O_4)

Bulk material and ceramically prepared NPs usually have about 20% of the Fe^{3+} cations located in the tetrahedral A-sites ($i = 0.2$). Since the magnetic moments of Mn^{2+} and Fe^{3+} are both 5 μ_B , the net magnetic moments of the normal and the inverse structures are expected to be identical (5 μ_B at 0 K). However, in practice, the net magnetic moment is always about 4.6 μ_B near 0 K [51]. Single crystals of MnFe_2O_4 generally appear to obey the relation (26) [106].

$$m = 5 - 2i \quad (26)$$

Several explanations have been put forward to explain this. Šimša and Brabers suggested, based on high field susceptibility measurements, that the spin moments A and B sublattices of the inverse structure of a molecule MnFe_2O_4 are not co-linear, but that

the Mn^{2+} -spins in the B sublattice are canted to the direction of the total magnetization by about 53°. DFT calculations have suggested that the most stable MnFe_2O_4 structures have Mn^{2+} -ions at the A site in the high spin state ($\mu = 5 \mu_B$), whereas those at the B sublattice are in an intermediate spin state ($\mu = 3 \mu_B$) [107]. A more likely explanation is that oxidation of Mn^{2+} to Mn^{3+} is involved, leading to a structure that can be represented as $[\text{Mn}_{0.8}\text{Fe}_{0.2}]^A(\text{Mn}_{0.2}\text{Fe}_{0.2}\text{Fe}_{1.6})^B\text{O}_4$. This structure was supported by low-temperature spin-echo ^{55}Mn - and ^{57}Fe -NMR studies [52,104,105,108].

Similarly, it was demonstrated that the initial cation distributions of NPs prepared by wet co-precipitation of Fe^{2+} and Mn^{2+} and subsequent air oxidation at 343 K appeared to be different: $[\text{Mn}_{0.48}\text{Fe}_{0.32}]^A[(\text{Mn}_{0.06}\text{Mn}_{0.46}\text{Fe}_{0.46}\text{Fe}_{1.02})^B\text{O}_4$ [108]. Upon heating at 573 K, the cation distribution of this material changed irreversibly to become identical to that of ceramically prepared material. Chen et al. and Zhang et al. prepared similar systems by wet co-precipitation at 298 K followed by digestion at about 370 K for 2 h. The resulting compounds have been shown to have a metastable random cation distribution corresponding with the ratio of the Fe and Mn cations in the synthesis mixture [63,98]. Usually, the as-synthesized materials of aqueous co-precipitations have higher inversion degrees than ceramically prepared manganese ferrites. A 1/2 ratio Mn/Fe afforded systems with an initial high i value of 0.61–0.67 because the thermal energy at 298 K is insufficient for redistribution of the cations. This as-synthesized mixture appeared to contain both divalent and trivalent Mn. Upon heating of this mixture up to 873 K in a vacuum, the Mn^{3+} was reduced completely and irreversibly to Mn^{2+} , whereas no change of the oxidation state of Fe^{3+} was observed by EELS spectroscopy. In this way, equilibrium states at lower i -values were reached ($i = 0.29$ – 0.40 at 298 K) [63,98].

Heat treatment of the same as-synthesized Mn-ferrite in air can result in partial oxidation of Mn^{2+} to Mn^{3+} [63,109], which as shown by EXAFS studies, is accompanied by a relatively small change in the degree of inversion [42,110]. Since the Mn^{3+} shows a preference for the octahedral sites, Mn^{2+} -cations in the A-sites exchange with Fe^{3+} -cations in the B-sites upon oxidation to Mn^{3+} . This may result in the formation of non-stoichiometric ferrites, in which the positive charge of these structures is probably counterbalanced by some cation vacancies in the crystals [42,63,106,111]. From the magnetic moments of Fe^{3+} , Mn^{2+} , and Mn^{3+} (5, 5, and 4 μ_B , respectively), it follows that the net magnetic moment per molecule decreases, which agrees well with the experimentally determined decrease in σ_S with the oxidation, which for particles of the same size is also reflected in a decrease in r_2 [42,63,112].

A polycrystalline microparticulate sample of Mn-ferrite that was obtained by a heat treatment at 1400 °C for 24 h followed by quenching in water adopted a normal spinel structure ($i = 0.2$) and can be described as $[\text{Mn}_{0.8}\text{Fe}_{0.2}]^A(\text{Mn}_{0.2}\text{Fe}_{1.8})^B\text{O}_4$. Non-hydrolytic thermal decomposition of metal-complexes typically resulted in high purity magnetic cores with controllable particle sizes and higher magnetization than for hydrolytically prepared ferrites [53]. In this way, a series of NPs of high quality single crystalline metal spinel ferrites MFe_2O_4 ($\text{M} = \text{Mn}^{2+}$, Fe^{2+} , Cu^{2+} , Ni^{2+}) was prepared [53]. The MnFe_2O_4 NPs with a size of 12 nm had an σ_S value of 79 $\text{A m}^2 \text{kg}^{-1}$, which is higher than the σ_S for Fe_3O_4 NPs of the same size (73 $\text{A m}^2 \text{kg}^{-1}$) and about the same as bulk MnFe_2O_4 (80 $\text{A m}^2 \text{kg}^{-1}$) [47].

In Table 1, relaxivities reported for single domain MnFe_2O_4 NPs are compiled together with the parameters that govern their magnitude. These NPs all have $d \leq 21$ nm. From Fig. 9, it can be concluded that the transverse relaxivity is in the MAR. With these NPs, r_2 values up to 450 s^{-1} mM can be reached. The trends in r_2 are roughly in agreement with those calculated using Eq. (12) (see Fig. 11). In these calculations, the effects of the coating, which

Table 1
Diameters, saturation magnetization, and relaxivities of MnFe₂O₄ NPs.

Coating ^a	d_{TEM} (nm) ^b	d_{DLS} (nm) ^c	σ_s (Am ² kg ⁻¹) ^d	T (K) ^e	B_0 (T) ^e	r_1 (s ⁻¹ mM ⁻¹) ^f	r_2 (s ⁻¹ mM ⁻¹) ^f	Ref.
PEG-PEI	3			RT	3		43	[113]
PEG-PEI	9			RT	3		57	[113]
PEG-PEI	18			RT	3		107	[113]
DMSA	6		49		1.5		208	[53]
DMSA	9		71		1.5		265	[53]
DMSA	12		79		1.5		358	[53]
PEG-PPG-PEG-di-succ	10	29	1.6	300	1.5		236	[114]
DMSA	7.6	215	53		9.4	18.6	228	[115]
TP80	12	41	40	298	1.5		384	[74]
DMSA	15		90	RT	4.5		422	[87]
TEG	7		39		0.5		126	[85]
Au@CTAB	12				1.5	4.0	56	[116]
CTAB	8.6		55	293	9.4		197	[42]
CTAB	8.2		66	293	9.4		346	[42]
Citric acid	18	95	76	310	1.5	19.0	394	[76]
DA-PEG ₁₀₀₀	6	11	48	RT	1.5		249	[80]
DA-PEG ₂₀₀₀	6	13	48	RT	1.5		249	[80]
DA-PEG ₅₀₀₀	6	19	48	RT	1.5		199	[80]
DA-PEG ₁₀₀₀₀	6	23	48	RT	1.5		189	[80]
DA-PEG ₂₀₀₀₀	6	27	48	RT	1.5		189	[80]
DA-PEG ₁₀₀₀	12	22	88	RT	1.5		448	[80]
DA-PEG ₂₀₀₀	12	24	88	RT	1.5		449	[80]
DA-PEG ₅₀₀₀	12	29	88	RT	1.5		400	[80]
DA-PEG ₁₀₀₀₀	12	35	88	RT	1.5		298	[80]
DA-PEG ₂₀₀₀₀	12	42	88	RT	1.5		288	[80]
Gal-PEG ₃₀₀₀	6	20	36	298	1.5	13.3	65	[81]
Gal-PEG ₃₀₀₀	7.5	23	43	298	1.5	18.6	88	[81]
Gal-PEG ₃₀₀₀	9	25	52	298	1.5	12.3	104	[81]
Gal-PEG ₃₀₀₀	12	31	66	298	1.5	7.4	174	[81]
Gal-PEG ₃₀₀₀	14	32	77	298	1.5	14.4	301	[81]
Gal-PEG ₃₀₀₀	6	20	36	298	9.4	0.8	63	[81]
Gal-PEG ₃₀₀₀	7.5	23	43	298	9.4	1.3	102	[81]
Gal-PEG ₃₀₀₀	9	25	52	298	9.4	0.9	137	[81]
Gal-PEG ₃₀₀₀	12	31	66	298	9.4	2.3	262	[81]
Gal-PEG ₃₀₀₀	14	32	77	298	9.4	1.3	336	[81]
CTAB	21		6.3	298	1.5		110	[117]
NDOPA-PEG ₆₀₀	7.8		61	RT	3		448	[79]
Phosphorylated mPEG ₂₀₀₀₀	2	8	19	300	3	8.4	21	[86]
Phosphorylated mPEG ₂₀₀₀₀	3	9	25	300	3	8.2	22	[86]
Phosphorylated mPEG ₂₀₀₀₀	3.9	13	29	300	3	7.0	27	[86]
PEG ₄₀₀	6.4		34	310	9.4	0.7	118	[66]
DHCA	3	14	43	300	7		125	[69]
DHCA	8	32	75	300	7		241	[69]
DHCA	3.9		21	RT	7	6.7	27	[118]
CREKA	4.1		19	RT	7	6.8	25	[118]
mPEG ₁₀₀₀	3.1		26	300	3	9.9	23	[119]
PEG6000	47.8		78		1.5	1.24	61	[120]
CTAB	19.5		59	RT	1.5		296	[82]

^a CREKA = Cys-Arg-Glu-Lys-Ala; CTAB = cetyltrimethylammonium bromide; DA = dodecanoic acid; DHCA = 3,4-dihydroxyhydrocinnamic acid; DMSA = 2,3-dimercaptosuccinic acid; mPEG = methoxy polyethylene glycol; NDOPA-PEG = nitrodopamine-polyethylene glycol-carboxylate; PEG = polyethylene glycol; gal = gallol; PEI = poly(ethylene imine); PEG-PPG-PEG-di-succ = disuccinate of poly(ethylene glycol)-block-poly(propylene glycol)-block-poly(ethylene glycol); TEG = tetraethylene glycol; TP80 = tri-aminated polysorbate 80.

^b Diameter of core as determined by TEM.

^c Hydrodynamic diameter as determined by DLS.

^d Expressed per mass bare MnFe₂O₄. Values reported as expressed per mass Mn(+Fe) atoms were corrected.

^e Magnetic field strength or temperature at which the relaxivities were measured

^f Expressed per mM of Mn + Fe

are difficult to predict, were not taken into account. It is noticeable that all but one experimental values are higher than the calculated ones. Possibly, this may be attributed to the effect of the coatings. If the coatings were impermeable to water, the opposite effect would be expected according to Eq. (19). Probably almost all applied coatings were at least partly permeable. Possibly, the coatings increased the ordering at the core surface, which would lead to a rise in σ_s and thus also in r_2 . Other possible r_2 increasing effects may be due to significant inner-sphere contributions by water or proton exchange between the coating and the bulk and to a local decrease of τ_D in the coating.

3.3.2. Non-stoichiometric manganese ferrites (Mn_xFe_{3-x}O₄)

Relaxivities of non-stoichiometric manganese ferrites and parameters on which they depend are summarized in Table 2. Several groups have reported that the σ_s of Mn_xFe_{3-x}O₄ NPs as a function of x has a maximum at $x \approx 0.4$ – 0.6 (see Fig. 12) [119,121–124]. For example, spherical Mn_xFe_{3-x}O₄ NPs with a diameter of about 18.5 nm, prepared by a thermal decomposition method of metal oleates, exhibited an almost linear increase in σ_s from 50.8 to 89.5 A m² kg⁻¹ (mass of Fe + O) at 300 K between $x = 0$ and $x = 0.43$ (see Fig. 12) [122]. The σ_s values for systems with x between 0 and 0.43 varied almost linearly (see Fig. 12) [122]. Fer-

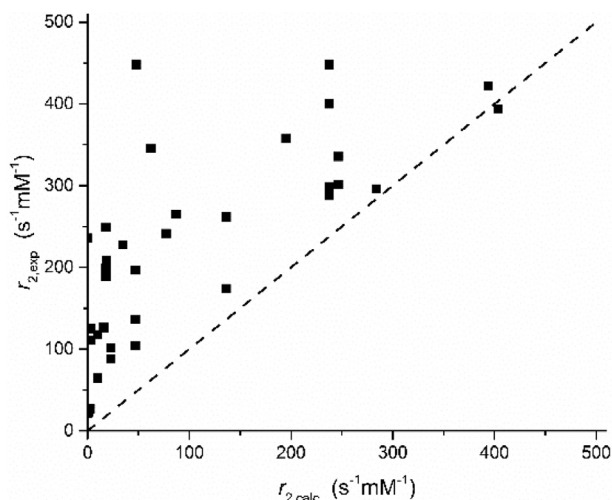


Fig. 11. Comparison of experimental r_2 values for MnFe_2O_4 NPs (see Table 1) with results of calculations from Eq. (12) using d -values of the cores, determined by TEM, $D = 2 \times 10^{-9} \text{ m}^2 \text{ s}^{-1}$, $\rho = 4.96 \text{ kgL}^{-1}$. The coating was not considered. The dashed line represents $r_{2,\text{exp}} = r_{2,\text{calc}}$.

rite ($x = 0$) adopts an inverse spinel structure ($[\text{Fe}^{3+}]^{\text{A}}(\text{Fe}^{2+}\text{Fe}^{3+})^{\text{B}}\text{O}_4$) and XRD indicates that this structure is maintained upon doping with Mn^{2+} . Since the Mn^{2+} ions prefer the tetrahedral A-sites, the structure of these $\text{Mn}_x\text{Fe}_{3-x}\text{O}_4$ NPs ($x = 0$ and $x = 0.43$) can be represented as $[\text{Mn}_x^2+\text{Fe}_{1-x}^{3+}]^{\text{A}}(\text{Fe}_{1-x}^{2+}\text{Fe}_{1+x}^{3+})^{\text{B}}\text{O}_4$. The spin-only moment for $0 \leq x \leq 1$ is $(x + 4) \mu_{\text{B}}$ at 0 K, which can account for the almost linear increase of σ_s that was observed between $x = 0$ and 0.43. However, further increase of x above 0.43 resulted in a gradual decrease in σ_s and it appeared that the σ - H curves did not saturate completely suggesting a paramagnetic contribution to the magnetization. This has been explained by lattice distortion as supported by XRD and HRTEM studies that indicate significantly increasing lattice distances and disturbance of lattice fringes at the higher x values [122]. Other possible reasons for the decrease in σ_s going from $x = 0.4$ to 1 have been suggested: (1) weakening of the AB interaction upon an increase of the ratio $\text{Fe}^{3+}/\text{Mn}^{2+}$ in the A-site [119,121], (2) random spin canting at the surface of the NPs due to reduced superspin exchange coupling [121,123]. Citrate coated particles with $x = 0.57$ exhibited a record high r_2 of $904 \text{ s}^{-1} \text{ mM}^{-1}$ at 7 T and 300 K, which is a factor of about 4 higher than for ferrite (Fe_3O_4). The r_2 values measured at a magnetic field strength of 0.5 T were about a factor 2 lower, whereas the reported σ - H curves showed that the corresponding σ -values differed by only a factor of about 1.1, based on which a difference in r_2 of only a factor of 1.3 would be expected assuming that the MAR regime is operative here (see Eq. (12)). This suggests that the inner-sphere contribution to the relaxivity is significant for these particles. The σ_s -value of $21.1 \text{ A m}^2 \text{ kg}^{-1}$ for the NPs with $x = 1.06$ [122] is much lower than the σ_s for $\text{Mn}_x\text{Fe}_{3-x}\text{O}_4$ NPs ($x = 1$ –1.12, $d = 3$ –6 nm) prepared by thermal decomposition of metal carbonyl complexes followed by oxidation ($\sigma_s = 42$ –44 $\text{A m}^2 \text{ kg}^{-1}$) [99,125] and of bulk MnFe_2O_4 or high-quality single crystals (80 and 79 $\text{A m}^2 \text{ kg}^{-1}$, respectively) [47,53]. This underlines once again that synthetic procedures are decisive for the magnitude of the magnetization of the products.

Similar trends in σ_s were observed for PEGylated $[\text{Mn}_x^2+\text{Fe}_{1-x}^{3+}]^{\text{A}}(-\text{Fe}_{1-x}^{2+}\text{Fe}_{1+x}^{3+})^{\text{B}}\text{O}_4$ NPs ($x = 0$ –0.34, core about 6 nm diameter) [124]. For these ultra-small NPs, the r_1 and r_2 values are of the same order of magnitude ($r_2 = 41$ –67; $r_2/r_1 = 2$ –3 at 1.5 T), which provides these materials with potential as dual-mode T_1/T_2 CA. Another series of $\text{Mn}_x\text{Fe}_{1-x}\text{Fe}_2\text{O}_4$ NPs (prepared by co-precipitation) has been reported to have about the same or somewhat lower σ_s values than SPION NPs, but surprisingly their r_2 values were a factor 4 higher

[126]. In the long term, these NPs appeared to aggregate, which may explain these high r_2 values. The aggregation could be avoided by surface coating with sodium tricitrate [127].

Oxidation of Mn^{2+} to Mn^{3+} may disturb the trend described above, because of the lower magnetic moment of the latter ($4 \mu_{\text{B}}$ as compared to $5 \mu_{\text{B}}$ for Mn^{2+}). The positions of the Fe- and Mn-edge peaks in the XANES spectra of $\text{Mn}_x\text{Fe}_{3-x}\text{O}_4$ NPs prepared by hydrothermal decomposition of $\text{Fe}(\text{acac})_3$ and $\text{Mn}(\text{acac})_2$ under an inert gas (Ar) have indicated the presence of considerable amounts of Mn^{3+} and Fe^{2+} [112].

Tuning of the ratio Mn/Fe in Mn-ferrites prepared by thermal decomposition of $\text{Mn}(\text{acac})_2$ and $\text{Fe}(\text{acac})_3$ is difficult because the decomposition temperatures of these complexes differ significantly (522 and 459 K, respectively). Therefore, the simultaneous incorporation of Fe^{3+} and Mn^{2+} is often not possible without the formation of a second phase of, for example, MnO , which is washed out during subsequent washing procedures. Since $\text{Mn}(\text{acac})_3$ decomposes at about the same temperature as $\text{Fe}(\text{acac})_3$, it might be a more suitable precursor than $\text{Mn}(\text{acac})_2$ in the preparation of $\text{Mn}_x\text{Fe}_{3-x}\text{O}_4$ NPs. A series of $\text{Mn}_x\text{Fe}_{3-x}\text{O}_4$ NPs ($x = 0.29$ –0.77, core diameter 5–6.5 nm) has been prepared by decomposition of $\text{Mn}(\text{acac})_3$ and $\text{Fe}(\text{acac})_3$ in a molar ratio 1:2 using a polyol as the solvent, which served also as a mild reducing agent for the Mn^{3+} as well as for the surface coating of the NPs. The x -value of the product was dependent on the choice of the polyol [110,129]. It was assumed that Mn^{3+} is almost completely reduced under the conditions applied whereas Fe^{3+} is not. There will likely be vacancies to ensure that there is no excess positive charge on the spinel framework. A structure with $x = 0$ would resemble maghemite, which can be considered as an Fe^{2+} -deficient magnetite with 1/3 vacancy. The σ - H curves showed a clear saturation and no paramagnetic contribution. Mn^{2+} appeared to be located mainly in the A-sites. A maximum magnetization at $\sigma_s = 80.3 \text{ A m}^2 \text{ kg}^{-1}$ (at 300 K) was observed for NPs with $x = 0.35$. However, the highest r_2 was observed for NPs with $x = 0.77$. This has been explained by the formation of aggregates in this sample as witnessed by dynamic light scattering (DLS) [110]. In a recent study on 8.5 nm NPs of metal-doped ferrites prepared by solvothermal decomposition of metal acetylacetonates, the variations of σ_s -values of $\text{Mn}_x\text{Fe}_{3-x}\text{O}_4$ complexes with x were relatively small; a vague maximum was observed for $x = 0.7$ ($\sigma_s = 78 \text{ A m}^2 \text{ kg}^{-1}$ at 300 K) [128]. Co-doping with Zn^{2+} resulted in an increase of σ_s to up to $125 \text{ A m}^2 \text{ kg}^{-1}$ for $\text{Zn}_{0.12}\text{Mn}_{0.26}\text{Fe}_{2.62}\text{O}_4$ (see also section 3.3.3). These NPs were coated with a dodecylamine modified (isobutylene-*alt*-maleic anhydride) polymer. The r_2 values were only modest (21 – $72 \text{ s}^{-1} \text{ mM}^{-1}$ at 3 T and 300 K) and they did not reflect the trends observed in σ_s -values. Possibly, the relatively low r_2 can be ascribed to impermeability of the applied polymeric coating layer to water.

Preparation by co-precipitation afforded $\text{Mn}_x\text{Fe}_{3-x}\text{O}_4$ NPs with a diameter of about 20 nm that showed a linear decrease in σ_s from 86.0 to 4.6 $\text{A m}^2 \text{ kg}^{-1}$ between $x = 0$ and 0.75 [130]. At the same time, the Curie temperature decreased from 610 to 510 K, suggesting that the AB-superoxchange energy is decreasing upon replacement of Fe^{2+} by Mn^{2+} .

Other preparation procedures generally result in materials with lower σ_s values and thus lower r_2 values. Contamination with other metal ions and partial oxidation may influence σ_s as well.

3.3.3. Manganese ferrites doped with zinc ($\text{Zn}_x\text{Mn}_{1-x}\text{Fe}_2\text{O}_4$)

Doping of Mn^{2+} with another metal ion that has a lower magnetic moment including Mn^{3+} [42] Fe^{2+} , and Zn^{2+} has substantial effects on the magnitude of σ_s because these cations change the antiferromagnetic superexchange interaction between the A-sites and the B-sites [87]. EXAFS spectra indicated that the divalent metal ions prefer the tetrahedral A sites and the substitution of

Table 2Diameters, saturation magnetization and relaxivities of $\text{Mn}_x\text{Fe}_{3-x}\text{O}_4$ NPs.

x	Coating ^a	d_{TEM} (nm) ^b	d_{DLS} (nm) ^c	σ_s ($\text{Am}^2\text{kg}^{-1}$) ^d	T (K) ^e	B_0 (T) ^e	r_1 ($\text{s}^{-1}\text{mM}^{-1}$) ^f	r_2 ($\text{s}^{-1}\text{mM}^{-1}$) ^f	Ref.
1.12	None	3		44	310	3	1.97	15	[125]
1.13	None	4.6		43.2	310	3	1.49	18	[125]
1.09	None	4.8		42	310	3	0.84	50	[125]
1.12	None	5.9		44	310	3	0.68	98	[125]
0.6	DMSA	9.3		52.8 ^g	313	0.47		220	[90]
0.6	DMSA	12.5		75.0 ^g	313	0.47		379	[90]
0.6	DMSA	16.3		84.7 ^g	313	0.47		420	[90]
0.29	PEG ₈₀₀₀	6.5	215	65.6	300	9		32.7	[110]
0.35	PG	6.0	160	80.3	300	9		64.5	[110]
0.57	TEG&PG	5.8	140	75.7	300	9		126.5	[110]
0.77	TEG	5.0	765	60.3	300	9		212.2	[110]
0	Na ₃ citrate	11.90		67.63	295	1.5		57.0	[126]
0.24	Na ₃ citrate	7.80		62.40	295	1.5		236.6	[126]
0.47	Na ₃ citrate	7.40		60.55	295	1.5		203.9	[126]
0.70	Na ₃ citrate	9.62		71.13	295	1.5		202.1	[126]
0.25	Na ₃ citrate	6.8	72.4	55.4	295	1.5		239.5	[127]
0.50	Na ₃ citrate	7.4	85.6	58	295	1.5		203.4	[127]
0.75	Na ₃ citrate	9.4	105.2	58.8	295	1.5		184.6	[127]
0	Na ₃ citrate	18.5	22.1	50.8 ^h	300	7		244.2	[122]
0.09	Na ₃ citrate	18.5	21.4	60.1 ^h	300	7		397.1	[122]
0.19	Na ₃ citrate	18.5	21.2	67.7 ^h	300	7		512.5	[122]
0.31	Na ₃ citrate	18.5	22.4	73.3 ^h	300	7		715.6	[122]
0.39	Na ₃ citrate	18.5	21.8	83.9 ^h	300	7		855.3	[122]
0.43	Na ₃ citrate	18.5	20.0	89.5 ^h	300	7		904.4	[122]
0.47	Na ₃ citrate	18.5	21.4	75.6 ^h	300	7		748.4	[122]
0.53	Na ₃ citrate	18.5	19.8	69.9 ^h	300	7		591.3	[122]
0.61	Na ₃ citrate	18.5	18.8	60.9 ^h	300	7		460.0	[122]
0.79	Na ₃ citrate	18.5	25.2	44.0 ^h	300	7		289.5	[122]
0.92	Na ₃ citrate	18.5	24.7	35.2 ^h	300	7		236.4	[122]
1.06	Na ₃ citrate	18.5	23.2	21.2 ^h	300	7		139.1	[122]
0.32	mPEG ₁₀₀₀	3.11		21.78	300	3	7.02	25.95	[119]
0.37	mPEG ₁₀₀₀	2.95		31.07	300	3	7.08	30.11	[119]
0.75	mPEG ₁₀₀₀	3.28		26.92	300	3	10.35	26.06	[119]
1	mPEG ₁₀₀₀	3.05		25.59	300	3	9.91	23.24	[119]
1.23	mPEG ₁₀₀₀	3.07		10.69	300	3	9.23	21.18	[119]
1.57	mPEG ₁₀₀₀	3.14		8.2	300	3	7.64	17.97	[119]
0.48	Dam-PMA	8.8	30	76	300	3		21	[128]
0.69	Dam-PMA	8.4	18	78	300	3		47	[128]
0.72	Dam-PMA	8.2	21		300	3		69	[128]
0.95	Dam-PMA	8.8	29	68	300	3		72	[128]

^a Dam-PMA = dodecylamine modified poly(isobutylene-alt-maleic anhydride) (6 kDa); DMSA = 2,3-dimercaptosuccinic acid; mPEG = methoxy polyethylene glycol; PEG = polyethylene glycol; PG = propylene glycol; TEG = tetraethylene glycol.

^b Diameter of the core as determined by TEM.

^c Hydrodynamic diameter as determined by DLS.

^d Expressed per mass bare MnFe_2O_4 unless stated otherwise.

^e Magnetic field strength or temperature at which the relaxivities were measured.

^f Expressed per mM of Mn + Fe.

^g At 300 K.

^h Expressed per mass Fe + O atoms.

Mn^{2+} in the normal spinel of MnFe_2O_4 with diamagnetic Zn gives a mixed ferrite $[\text{Zn}_x\text{Mn}_{1-x}]^{\text{A}}(\text{Fe}_2)^{\text{B}}\text{O}_4$ ($x = 0-1$). In this case, part of the antiferromagnetic coupling between Mn^{2+} in the A-sites and Fe^{3+} -ions in the B-sites is removed. The magnetic moment of the A-site is $(1-x)5 + 0 \mu_B$ and that of the B-site $5 + 5 \mu_B$ and since the moments of the A- and B-sites are anti-parallel, the net magnetic moment of the ferrite increases according to $5 + 5x$ at 0 K. This trend is in agreement with the curve of σ_s versus the level of Zn^{2+} doping at 300 K (Fig. 13, Table 3), which rises between $x = 0$ and 0.4, where it reaches a maximum in σ_s . At higher Zn^{2+} ion levels ($x > 0.4$) antiferromagnetic A-B coupling interactions are probably becoming so weak that the negative BB interaction comes into play, finally resulting in antiparallel Fe^{3+} moments on B sites and no net moment at 0 K for $x = 1$ (pure ZnFe_2O_4). Since r_2 is proportional to σ_s , the r_2 values of $(\text{Zn}_x\text{Mn}_{1-x})\text{Fe}_2\text{O}_4$ spinels exhibit a very high maximum of $860 \text{ s}^{-1} \text{ mM}^{-1}$ at $x = 0.4$ for NPs with a diameter of 15 nm [87]. The NPs mentioned were prepared by employing a thermal decomposition method with slow growth of nanocrystals at 573 K. A similar trend was observed with 8 nm

NPs that were also prepared by thermal decomposition followed by coating with nitrodopamine conjugated polyethylene glycol-600 (NDOPA-PEG₆₀₀). Those NPs had a maximum σ_s and r_2 for $x \approx 0.2$ ($110 \text{ A m}^2 \text{ kg}^{-1}$ and $552 \text{ s}^{-2} \text{ mM}^{-1}$ at room temperature and 3 T) [79]. Mixed Zn-Mn ferrites prepared by a hydrothermal precipitation method (at 453 K) showed, at room temperature, curves with a smooth decrease of σ_s from about 65 to $20 \text{ A m}^2 \text{ kg}^{-1}$ between $x = 0$ and 1, without a maximum [131,132]. This has been ascribed to the formation of a metastable distribution of the metal ions over the A- and the B-sub-lattices, at the relatively low preparation temperature. A Mössbauer spectroscopy study on 12 nm $\text{Mn}_{0.65}\text{Zn}_{0.35}\text{Fe}_2\text{O}_4$ has indicated that an irreversible phase transition to a stable phase occurs by cation rearrangement upon heating above about 500 K [133].

An alternative rationalization might be a preference for the normal spinel structure at $x < 0.6$, which would be in line with the degree of inversion of MnFe_2O_4 , which is 0.2 [46]. Large particles ($>100 \text{ nm}$) prepared by co-precipitation followed by calcining at 1373 K showed a similar trend [134]. From the fitting of the depen-

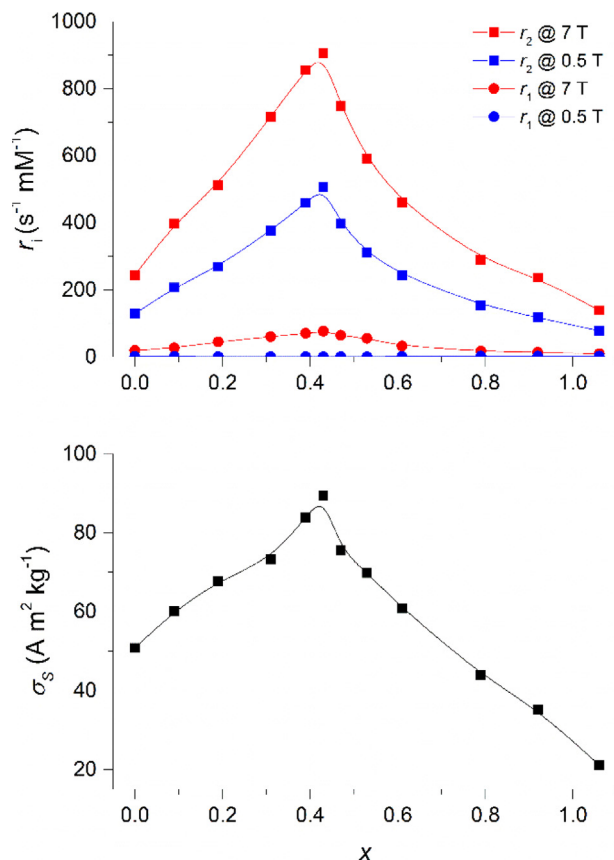


Fig. 12. Magnetization and relaxivity data of $\text{Mn}_x\text{Fe}_{3-x}\text{O}_4$ as a function of x at 300 K. Data from Ref. [122]. The σ_s values are expressed per kg Fe + O.

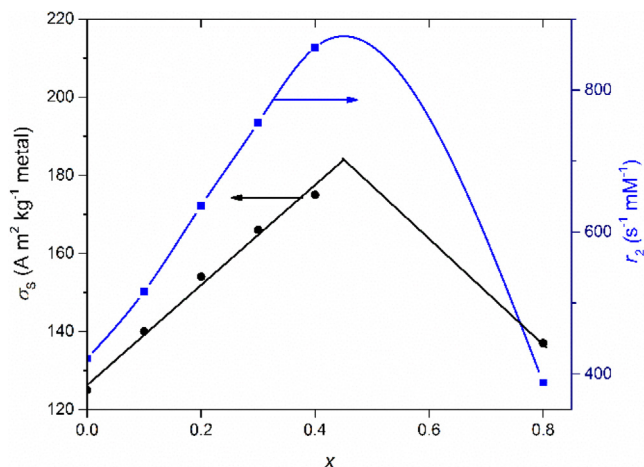


Fig. 13. Plot of σ_s at RT and r_2 at 4.5 T and RT as a function of the Zn-doping degree (x) in 15 nm NPs of $\text{Mn}_{1-x}\text{Zn}_x\text{Fe}_2\text{O}_4$. Constructed with data from ref. [87]. The lines are intended only as guides for the eye.

dencies of the magnetic moments of these particles as a function of x to quantum mechanical models, it was concluded that the preference of Zn^{2+} moves from location at site A to site B at $x = 0.4$.

$\text{Zn}_x\text{Mn}_{1-x}\text{Fe}_2\text{O}_4$ NPs (diameter 10 nm) prepared at relatively low temperatures by a hydrothermal procedure showed a weak maximum σ_s at $x \approx 0.4$ and a steep decrease between $x = 0.4$ and 0.6, but between $x = 0$ and 0.4, σ_s was almost invariable [131]. It was suggested that this behavior is also due to a meta-

stable distribution of the metal cations over the A- and B-sites with Zn^{2+} also located in the B-sites.

Fairly high σ_s ($98 \text{ A m}^2 \text{kg}^{-1} \text{Fe}$ for uncoated material) and r_2 ($338 \text{ s}^{-1} \text{mM}^{-1} \text{Fe}$) has also been achieved with monodisperse lipid-PEGylated Mn-Zn ferrite NPs with a shell-core structure [135]. This material has been used as a basis for theranostic agents.

Generally, the Curie temperature (T_C) of a manganese ferrite reduces with Zn-doping. This can be exploited in the design of self-regulation agents for hyperthermia, which have a Curie temperature slightly above physiological temperature and, therefore, lose the magnetization and their heating effect as soon as the temperature rises above T_C [136,137].

Reported transverse relaxivities and saturation magnetization of Zn-doped Mn-ferrite NPs of various sizes are compiled in Table 3.

3.4. Influence of the shape of the nanoparticles

Vuong et al. have shown by Monte Carlo simulations that the shape of NPs also affects their magnetic properties. In the MAR, spherical superparamagnetic NPs are more effective T_2 CAs than linear ones, whereas, in the SDR, the shape has not much effect on the transverse relaxivity [140]. However, an experimental study on Mn-ferrites covered with oleic acid suggests that truncated octahedral nanostructures possess lower and plates possess higher σ_s values and r_2 values [141]. Replacement of the oleic surface layer of these plates by more water-soluble FA-Gd(DTPA)-PEG-DIB chains resulted in a decrease in σ_s , most likely due to a decrease in Fe content of the particles, but the r_2 value rose significantly [141]. Possibly this can be ascribed to an exchange contribution to the relaxivity by the Gd^{3+} -chelates. An investigation on the doping of SPIO particles by ion exchange with Mn^{2+} and Zn^{2+} showed that the σ_s values of the resulting NPs (covered with citrate) were strongly dependent on their shapes. For NPs with Mn/Fe = 1/13–15, the order of the magnitudes of both σ_s and the corresponding r_2 values was octapods > cubes > spheres (see Fig. 14) [142]. Surprisingly, the same authors reported, for similar particles with an Mn/Fe molar ratio of 1/5, that the order of σ_s and r_2 was cubes \approx octapods > plates [143]. It should be noted that it is not clear whether in the above studies the NPs have the same volumes and whether canting effects can be excluded. Another study on various shapes of MnFe_2O_4 showed the order: needles ($400 \times 8 \text{ nm}$) > rods ($800 \times 30 \text{ nm}$) > wires ($1000 \times 35 \text{ nm}$) [144].

3.5. Effects of coating and attachment of targeting vectors

Coating of NPs is essential for their colloidal stability under physiological conditions [67]. NPs prepared by ceramic methods or by solvothermal procedures in an organic solvent are hydrophobic. Often oleic acid and oleylamine are applied during these procedures. Ligand exchange and/or coating with a hydrophilic compound is required to make the NPs dispersible in an aqueous medium. Moreover, a surface coating can be used to reduce the toxicity by preventing leaching of metal ions, to control biodistribution, to hide NPs from the immune system, and to serve as an anchor for targeting vectors. Coating of a bare Mn-ferrite NP generally will result in a decrease of its σ_s . As stated above (see Eqs. (19) and (20)), a water-impermeable coating decreases the transverse relaxivity in the MAR but does not affect it outside this regime, obviously provided that after the coating, the system does not move from the SDR into the MAR. However, a different situation arises when the surface bonding chemistry influences the spin disorder at the surface, for example by occupying the missing O-atoms and thus reducing the disorder. Since then the surface resembles more the core, the thickness of the dead layer decreases, and usually also the paramagnetic contribution to the magnetiza-

Table 3
Diameters, saturation magnetization and relaxivities of $Zn_xMn_{1-x}Fe_2O_4$ NPs.

X	Coating ^a	d_{TEM} (nm) ^b	d_{DLS} (nm) ^c	T (K) ^d	B_0 (T) ^d	σ_s ($A m^2 kg^{-1}$) ^e	r_2 ($s^{-1} mM^{-1}$) ^f	Ref.
0	DMSA	15			4.7	125 ^g	422	[87]
0.1	DMSA	15			4.7	140 ^g	516	[87]
0.2	DMSA	15			4.7	154 ^g	637	[87]
0.3	DMSA	15			4.7	166 ^g	754	[87]
0.4	DMSA	15	17		4.7	175 ^g	860	[87]
0.8	DMSA	15			4.7	137 ^g	388	[87]
0.72	DMSA	10		295	1.5	30 ^h	125	[138]
0.1	None	7.7		RT	3	95		[79]
0.4	None	7.7		RT	3	89		[79]
0.2	NDOPA-PEG ₂₀₀	7.7	22	RT	3	110	250	[79]
0.2	NDOPA-PEG ₄₀₀	7.7	25	RT	3	110	433	[79]
0.2	NDOPA-PEG ₆₀₀	7.7	34	RT	3	110	552	[79]
0.2	NDOPA-PEG ₂₀₀₀	7.7	47	RT	3	110	194	[79]
0.5	None ⁱ	8.0	20.3	RT	1.5	42	263	[139]
0.5	Fe ₃ O ₄ ⁱ	10.0	27.0	RT	1.5	49	323	[139]
0.5	Fe ₃ O ₄ ⁱ	12.3	28.6	RT	1.5	53	286	[139]
Zn _{0.12} Mn _{0.26} Fe _{2.6} O ₄	Dam-PMA	8.5	21	RT	3	93	65	[128]
Zn _{0.15} Mn _{0.55} Fe _{2.3} O ₄	Dam-PMA	8.5	26	RT	3	82	51	[128]

^a Dam-PMA = dodecylamine modified poly(isobutylene-alt-maleic anhydride) (6 kDa); DMSA = 2,3-dimercaptosuccinic acid; NDOPA-PEG = nitrodopamine-polyethylene glycol-carboxylate.

^b Diameter of the core as determined by TEM.

^c Hydrodynamic diameter as determined by DLS.

^d Magnetic field strength or temperature at which the relaxivities were measured.

^e Expressed per mass bare $Zn_xMn_{1-x}Fe_2O_4$ unless stated otherwise.

^f Expressed per mM of Mn + Fe.

^g Expressed per mass Fe + O atoms.

^h The best-fit value obtained by fitting of reported σ -H curve after rescaling of the σ -scale by a factor of 10.

ⁱ Acid peptized

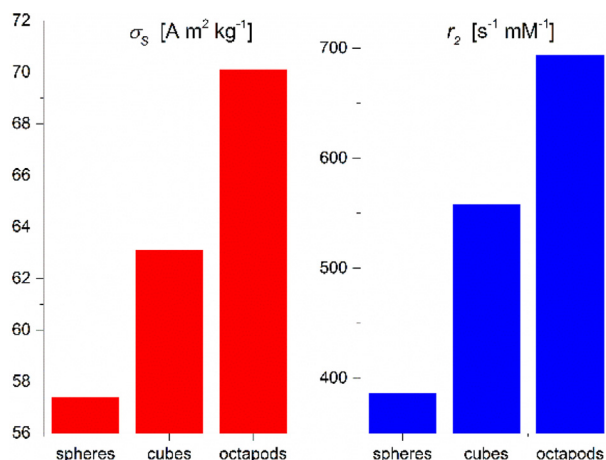


Fig. 14. The effect of the shape on σ_s and r_2 of Mn-doped USPIO particles. Mn/Fe ratios: spheres 1/12, cubes 1/13, octapods 1/15 with diameters of 17, 23, 32 nm as measured by TEM, respectively. Temperature 310 K. The r_2 values were measured at 7 T. Data from ref. [142].

tion [60,78,145]. In that case σ_s and r_2 may increase. Moreover, surface coating with ligands having exchangeable protons may give rise to a significant exchange contribution to both the longitudinal and transverse relaxivity. Surface coatings that require basic reaction conditions may promote oxidation of the Mn^{2+} in the core and thus lower the σ_s [146].

The effect of the coating of $MnFe_2O_4$ NPs (6 and 12 nm diameter) with a series of amphiphilic dodecanoic-PEG block polymers of molecular weights between 1 and 20 K has been investigated systematically (see Table 1) [80]. For both particle sizes, r_2 as a function of the molecular weight of the coating polymer started to decrease steeply above 2 K. Possibly this is due to a reduction of the permeability of the coating for water at high MWs, due to a

changeover of the conformation of the dodecanoic-PEG chains from the mushroom regime with folded chains in a relatively thin layer to the brush regime with unfolded chains in a thick and less water-permeable layer. A similar effect has been observed recently with PEGylated zeolite NPs [147]. Likewise, $Zn_{0.2}Mn_{0.8}Fe_2O_4$ NPs having a core diameter of 8 nm and coated with NDOPA-PEG_n of various PEG chain lengths showed a maximum in r_2 for $n = 600$ Da ($r_2 = 552 s^{-1} mM^{-1}$ at 3 T and room temperature, see Table 3) [79].

Encapsulation of polycrystalline $MnFe_2O_4$ NPs (100–150 nm diameter) in a mesoporous silica layer of 20–25 nm thickness followed by attachment of folic acid through an aminopropyl-silica linker afforded a targeting T_2 CA [148]. The σ_s value decreased with the two consecutive coating steps from 95 to 99 $A m^2 kg^{-1}$ to successively 73–75 and 60–63 $A m^2 kg^{-1}$. The mesoporous silica layer can be exploited as a drug carrier, as was demonstrated for the anti-cancer drug doxorubicin. Other theranostic NP-systems were prepared by first coating $MnFe_2O_4$ NPs with meso-2,3-dimercaptosuccinic acid (DMSA) [115]. In the next step, chitosan was attached covalently to the DMSA of such NPs. The free ammonium groups of chitosan were then available for transport of negatively charged drugs. In this way, multimodal theranostics (MRI/drug delivery/hyperthermia therapy) were obtained [149]. The σ_s value (normalized by the total sample weight) decreased with increasing thickness of the coating, which was ascribed to spin canting effects due to the coating of the surface.

Covering Mn-ferrite NPs with a layer of Fe_3O_4 has advantages for application in hyperthermia therapy. The core-shell interaction between the two magnetic phases has a beneficial effect on the heating efficiency of this type of NPs [150]. Superparamagnetic core-shell NPs $MnFe_2O_4@Fe_3O_4$ with a diameter of 12.5 nm after coating with chitosan have been reported to display much higher r_2 values (184.1 $s^{-1} mM^{-1}$ Fe at 9.4 T and 298 K) than monophasic NPs of comparable size (96.6 and 83.2 $s^{-1} mM^{-1}$ Fe for Fe_3O_4 a $MnFe_2O_4$, respectively), although the saturation magnetization of all these NPs was about the same (62–69 $A m^2 kg^{-1}$ at 298 K) [83].

Covering of $\text{Zn}_{0.5}\text{Mn}_{0.5}\text{Fe}_2\text{O}_4$ NPs with a shell of Fe_3O_4 resulted in a decrease of σ_s at 10 K but the value of σ_s of the core-shell system at 300 K was up to 25% higher than that of the core alone (see Table 2) [139]. This effect was ascribed to exchange coupling between the core and the shell, which was assumed to be ferrimagnetic at 10 K and ferromagnetic at 300 K. As expected, the higher σ_s values for the $\text{Zn}_{0.5}\text{Mn}_{0.5}\text{Fe}_2\text{O}_4@ \text{Fe}_3\text{O}_4$ systems at 300 K resulted also in higher r_2 values. A significant increase of σ_s was also achieved by applying MnFe_2O_4 as a shell on a core of single-domain ferromagnetic elemental Fe [151]. The resulting $\text{Fe}@ \text{MnFe}_2\text{O}_4$ NPs (core diameter 12 nm, total diameter 16 nm) displayed an unusual σ - H curve with a negligible coercivity while the core alone had a significant coercivity, probably due to the dominance of the superparamagnetic contribution over the slow magnetization of the ferromagnetic core. At higher external magnetic field strengths, the core contribution became dominant resulting in an overall σ_s which is the volume average of the contributions of the core and the shell (149 $\text{A m}^2 \text{ kg}^{-1}$ at 300 K). This value is higher than those of Fe_3O_4 and MnFe_2O_4 NPs with the same particle size, which exhibited σ_s values of 95 and 101 $\text{A m}^2 \text{ kg}^{-1}$, respectively. Accordingly, these $\text{Fe}@ \text{MnFe}_2\text{O}_4$ NPs after making them aqueous dispersible by an additional coating with DMSA had a high transverse relaxivity ($r_2 = 356 \text{ s}^{-1} \text{ mM}^{-1}$ at 300 K). The latter coating allowed attachment of targeting vectors.

Coating of MnFe_2O_4 NPs (12 nm) with an aminated non-ionic surfactant polysorbitol 80 afforded a polycationic CA under physiologic conditions (see Table 1), which was taken up by cells probably through electrostatic interaction with the negatively charged cell membranes [74].

To increase stability and reduce toxicity, MnFe_2O_4 NPs have also been coated with Au (see Table 1) [116].

3.6. Clustering of manganese ferrite nanoparticles

Synthetic methods to prepare Mn-ferrite NPs, such as solvothermal decomposition of metal complexes and coprecipitation can be used to prepare NPs with sizes up to about 20 nm. Since the diameter of the NPs is one of the principal parameters that govern the transverse relaxivity, the clustering of these small NPs may be an attractive way to attempt to increase r_2 . Several ways of clustering Mn-ferrite NPs have been explored, including encapsulating dense clusters of single crystals in an impermeable coating (core-shell systems), embedding in micelles or liposomes, and attachment to solid supports. The resulting clusters all contain substantial amounts of diamagnetic material. Analysis of the literature data on the magnetic properties of such systems is complicated by the non-uniform way in which values of σ_s and r_2 are expressed in the literature. The magnetizations are expressed either for the whole cluster or for the composing small NPs. In both methods, the mass may be related either to (1) the whole particles (Mn-ferrite + all diamagnetic material), (2) Mn + Fe (+Zn), or (3) Fe. Often mass densities and the Mn-ferrites loading (wt %) of the clusters are not known, which makes interconversion between these unit systems impossible. In addition, the lack of knowledge on the water permeability of the nanoparticles makes it difficult to accurately determine their effective diameters. Relaxivities are expressed in $\text{s}^{-1} \text{ mM}^{-1}$ (Mn + Fe) but sometimes as $\text{s}^{-1} \text{ mM}^{-1}$ (Fe). Moreover, the magnetization may be affected by the clustering, for example by altering the thickness of the dead layer in the constituting single NPs or by oxidation of Mn^{2+} to Mn^{3+} during the cluster preparation.

Monte Carlo simulations have shown that compact clusters induce relaxation enhancements equivalent to similarly-sized single-crystal particles [152]. Therefore, for NPs that are in the MAR, the transverse relaxivity can also be increased by assembly to larger clusters, such as micelles, liposomes, or by embedding

them in gels. The cluster can be considered as a particle with a total magnetic moment as determined by Langevin's law (Eq. (22)). Consequently, the σ_s -values of the constituting small NPs effectively do not add up but the overall magnetization per weight bare ferrite remains the same, provided that magnetic interactions between the constituent NPs of the cluster are negligible. However, an increase in the number of NPs in a cluster (the loading density) determines the volume fraction f , which leads to an increase in r_2 [30]. Moreover, the diameter and thus τ_D increases upon clustering, which also contributes to an increase in r_2 . It should be noted the relaxivity increase would look less impressive if it were expressed per unit of mass rather than per mM [153].

At constant σ_s , r_2 will rise with d in the MAR, but after passing the border of the SDR, no further increase in r_2 or r_2^* will take place, and when, at even larger d , the PRR is reached r_2 will decrease, whereas r_2^* remains unchanged. (see Fig. 2). Besides the beneficial effect on the relaxivity, clustering will allow a high payload of paramagnetic ions and/or therapeutic drugs to be delivered to the site of interest, which will lead to an increased local concentration of these ions and therefore a high sensitivity. Another advantage of such an architecture may be the possibility of disintegration by bio-degradation, which may be less harmful to the body [77].

In Table 4, sizes, σ_s , and r_2 -values of clustered systems are compiled. From these values, it can be estimated that for the majority of these large particles $\tau_D \Delta \omega \geq 1$, which implies that they are in the MAR approaching the border with the SDR or in the SDR and, therefore, relatively high r_2 -values may be expected (see also Figs. 2 and 9). Nevertheless, only a few systems have r_2 values higher than $400 \text{ s}^{-1} \text{ mM}^{-1}$ (Mn + Fe). This can be explained by a low loading density or by the fact that the systems are under the PRR and not under the SDR. An easy but seldom performed check to discriminate between SDR and PRR is a comparison of r_2 and r_2^* . In the SDR these relaxivities are about equal, whereas in the PRR, $r_2^* > r_2$ with a gap between them that is dependent on τ_{CP} . This is nicely illustrated by Tromsdorf et al. for 6 nm Mn-doped ferrites (Mn/Fe = 0.12–0.32) embedded in micelles formed by a lipid (250 nm), which have $r_2 = 122$ and $r_2^* = 825 \text{ s}^{-1} \text{ mM}^{-1}$ (Fe) [113]. Here, it is evident that the PRR is operative. By contrast, encapsulating the same NPs into an amphiphilic polymer shell with a diameter of about 15 nm afforded $r_2 = 53$ and $r_2^* = 62 \text{ s}^{-1} \text{ mM}^{-1}$ (Fe).

The dramatic transverse relaxation enhancing effect by the increase in diameter due to clustering is demonstrated in an early example by Lee et al., who clustered spherical 12 nm MnFe_2O_4 NPs ($\sigma_s = 79 \text{ A m}^2 \text{ kg}^{-1}$; $r_2 = 358 \text{ s}^{-1} \text{ mM}^{-1}$) to spherical kernels with a diameter of 47.3 nm that were covered with a layer of SiO_2 and subsequently a layer of Au [154]. Due to these coating layers, the resulting NPs had diameters of 120 nm with an σ_s -value of only about $2 \text{ A m}^2 \text{ kg}^{-1}$, which should be expected because σ_s reduces with the third power of the diameter increase (see Eq. (25)). After PEGylation, the NPs had an r_2 of $465 \text{ s}^{-1} \text{ mM}^{-1}$ at 1.5 T. Based on these NPs a multifunctional targeting theranostic has been developed [154].

$\text{Mn}_{0.61}\text{Zn}_{0.42}\text{Fe}_{1.97}\text{O}_4$ NPs (10 nm diameter) have been encapsulated in silica. The resulting NPs consisted of a 26 nm diameter core of clustered ferrite, surrounded by a 19 nm thick silica coating [131,155]. The final system had a hydrodynamic diameter of 87 nm and $r_2 = 122 \text{ s}^{-1} \text{ mM}^{-1}$ Mn + Fe at 0.5 T and 310 K). Because the σ_s of these NPs showed a linear dependence on the temperature, whereas a quadratic decrease of the transverse relaxivity was observed in the range 70–5 °C, it was concluded that the system is in the MAR. Single particles coated with a monolayer of citrate showed a similar temperature dependency, whereas larger clusters covered with TiO_2 (hydrodynamic diameter 157 nm) showed an almost linear trend with the temperature, suggesting

Table 4
Diameters, saturation magnetization, and transverse relaxivities of clustered Mn-ferrite NPs.

Composing NPs		Clustered NPs							Ref.	
Mn/Fe	$d_{\text{TEM}}^{\text{a}}$ (nm)	Type ^b	Carrier/coating ^c	$d_{\text{TEM}}^{\text{a}}$ (nm)	$d_{\text{DLS}}^{\text{d}}$ (nm)	$\sigma_{\text{s}}^{\text{e}}$ (A m ² kg ⁻¹)	B_0 (T)	r_2^{f} (s ⁻¹ mM ⁻¹)		
0.32	4.5	C	PMA-TD		~15		3	32 ^g	[113]	
0.12	7.5	C	PMA-TD		~15		3	77 ^g	[113]	
0.32	4.5	M	Liposomes ^h		~250		3	94 ^g	[113]	
0.12	7.5	M	Liposomes ^h		~250		3	196 ^g	[113]	
0.5	12	C	SiO ₂ @Au(@PEG-COOH ₆₀₀₀)	47.3	120	2	1.5	465	[154]	
0.5	7.8	M	mPEG ₅₀₀₀ -b-PCL		80	65 ⁱ	1.5	270	[75]	
0.5	8	NG	PGA/PLL		222		4.7	437	[156]	
0.5	18.4	M	PBMA-g-C ₁₂ (5.6 wt%)		175	2.6	9.4	192 ^g	[161]	
0.5	18.4	M	PBMA-g-C ₁₂ (12.5 wt%)		146	4.8	9.4	226 ^g	[161]	
0.5	18.4	M	PBMA-g-C ₁₂ (25 wt%)		139	18.8	9.4	472 ^g	[161]	
0.5	18.4	M	PBMA-g-C ₁₂ (42.1 wt%)		132	32.5	9.4	633 ^g	[161]	
0.5	16.1	C	Thermolabile nanocapsules ^l	166	201	62 ^k	1.5	96–120 ^l	[45]	
0.5	9	M	C ₁₆ H ₃₃ -PMAA (pH = 4.5)		160	63 ^k	11.7	76	[77]	
0.5	9	M	C ₁₆ H ₃₃ -PMAA (pH = 7)		140	63 ^k	11.7	50	[77]	
0.5	9	M	P(MANa-co-DMA)	90–100	180	63 ^k	11.7	153	[77]	
0.5	9	M	P(ANa-co-DAAm)	45–65	130	63 ^k	11.7	129	[77]	
0.5	11.3	C	RITC@SiO ₂	60–80	80	62 ^m	9.4	596	[73]	
0.5	9	M	P(MANa-co-DMA-co-SDPQ)-g-PNIPAM		58	64	1.5	76	[71]	
0.5	8.2	C	SDS		75	105	93	47	[84]	
Mn _{0.6} Zn _{0.4} Fe ₂ O ₄	8	M	Star-block copolymer ⁿ		92	122	8.6	3	138 ^g	[157]
Mn _{0.4} Zn _{0.6} Fe ₂ O ₄	10	C	SiO ₂		65 ^o	0.5	0.5	300	[155]	
0.5	<15	C	SiO ₂		40	40	7.5	61	[162]	
0.15	5.78	S	GO-g-OAm		5.8	81	9.1	9.4	106 ^g	[158]
0.17	10.94	S	GO-g-OAm		10.9	90	13.1	9.4	228 ^g	[158]
0.10	13.93	S	GO-g-OAm		13.9	82	15.7	9.4	256 ^g	[158]
0.5	6	S	GO sheets		Sheet ^p	19	0.5	122 ^g	[159]	

^a Diameter as determined by TEM.

^b C = capsules or core-shell; M = micelles; NG = nanogel; S = NPs on support.

^c GO-g-OAm = graphene oxide grafted with oleylamine; mPEG = methoxy-PEG; P(ANa-co-DAAm) = copolymer of poly(sodium acrylate) and dodecyl acrylamide; PBMA-g-C₁₂ = poly(isobutylene-alt-maleic anhydride) grafted with dodecylamine; PCL = poly(ϵ -caprolactone); PEG = polyethylene glycol; PGA = poly(γ -glutamic acid); PLL = poly(L-lysine); PMAA = poly(methacrylic acid); P(MANa-co-DMA) = copolymer of poly(sodium methacrylate) and dodecyl methacrylate; P(MANa-co-DMA-co-SDPQ)-g-PNIPAM = poly(sodium methacrylate-co-dodecyl methacrylate-co-2,4-diphenyl-6-(4-vinylphenyl)quinoline) grafted with poly(N-isopropylacrylamide); PMA-TD = poly(maleic anhydride-alt-1-tetradecene) crosslinked by bis(6-aminohexyl)amine; RITC = rhodamine-B isothiocyanate; SDS = sodium dodecyl sulfate

^d Hydrodynamic diameter as determined by DLS.

^e Expressed per kg material, unless stated otherwise.

^f Expressed per mM (Fe + Mn) unless stated otherwise. Measured at 298–310 K.

^g Per mM Fe.

^h Liposome membrane: 78.4% 1,2,3-tri-(*cis,cis*-9,12-octadecadienyl)glycerol, 19.6% 1,2-diacyl-*sn*-glycero-3-phosphocholine and 2% 1-acyl-*sn*-glycero-3-phosphocholine.

ⁱ Per kg MnFe₂O₄.

^j Thermolabile nanocapsules prepared from hexadecanediol, toluene-2,4-diisocyanate, and 2,2'-Azobis[2-[1-(2-hydroxyethyl)-2-imidazolin-2-yl]propane] dihydrochloride.

^k Measured on composing single NPs.

^l Depending to the number of composing NPs in the cluster.

^m Per kg (Fe + Mn).

ⁿ Amphiphilic star-block polymer. For structure see Ref. [157], supporting information.

^o Diameter of resulting silica embedded ferrite clusters with cluster diameter of 26 nm.

^p Sheets: (70–110) × (0.8–1.1) nm.

that these particles were close to the SDR regime, which was supported by the relatively high r_2 (329 s⁻¹ mM⁻¹ Mn + Fe at 0.5 T and 310 K).

MnFe₂O₄ NPs (8 nm diameter) have been embedded into a gel matrix by coating them with poly-(γ -glutamic acid) followed by gelation with poly(L-lysine) [156]. The resulting NPs had a diameter of 222 nm with $r_2 = 436.8$ s⁻¹ mM⁻¹ at 4.7 T and room temperature, which is most likely in the PRR. By attachment of negatively charged quantum dots to these positively charged NPs, a bimodal MRI/NIR probe was constructed. Another example is the encapsulation of spinel NPs of Mn_{0.6}Zn_{0.4}Fe₂O₄ with a diameter of 8 nm ($\sigma_{\text{s}} = 60$ A m² kg⁻¹) in micelles of a spherical amphiphilic star-shaped copolymer with a diameter of 92 nm. The resulting system had $\sigma_{\text{s}} = 8.6$ A m² kg⁻¹ and $r_2 = 138$ s⁻¹ mM⁻¹ (Fe) at 1.5 T [157].

Various systems of clustered Mn- and Mn/Zn doped ferrite NPs have been embedded into micelles of amphiphilic compounds, often diblock copolymers [75,77,113,156]. Comparison of the reported σ_{s} and d data (Table 4, Fig. 9) suggests that the resulting micelles are often in the SDR or the PRR. Polymeric micelles formed

by self-assembly of MnFe₂O₄ NPs (7.8 nm diameter) by an amphiphilic diblock polymer with a hydrodynamic diameter of 79.6 nm had a σ_{s} value of 65 A m² kg⁻¹, which is somewhat lower than of a comparable monomeric system (74 A m² kg⁻¹) [75]. Thanks to the larger diameter, the r_2 measured with the polymeric system (270 s⁻¹ mM⁻¹) was much higher than a comparable monomeric system (66 s⁻¹ mM⁻¹). Menelaou et al. constructed magnetic colloids superparticles by assembly of 14–20 oleylamine-coated MnFe₂O₄ NPs (diameter 9 nm) into micelles of amphiphilic polymers to give micellar particles with hydrodynamic diameters of 130–180 nm [77]. They concluded that the relaxivity of these particles was in the SDR but from Fig. 9 and the relatively low r_2 -values (50–153 s⁻¹ mM⁻¹ at 11.7 T) suggest that here the PRR might be operative. The value of r_2 was dependent on the shape of the copolymer applied for the encapsulation; comb-shaped copolymers gave rise to higher r_2 values than a linear one.

Spherical MnFe₂O₄ NPs with a diameter of 11.3 nm have been assembled to a system with a core of about 50 nm, which was subsequently surrounded by two highly permeable mesoporous silica

shells: a fluorescent silica shell doped with rhodamine-B-isothiocyanate and a silica shell, without dye, to prevent photobleaching and to enhance the photo-stability. The resulting NPs have diameters of 60–80 nm with $\sigma_s = 62.45 \text{ A m}^2 \text{ kg}^{-1}$, which likely is in the SDR (see Fig. 9) and therefore, has a rather high r_2 ($598 \text{ s}^{-1} \text{ mM}^{-1} \text{ mM}^{-1}$). This material has potential as dual T_2 /optical imaging CA and also has good hyperthermia capabilities [73].

A spinel Mn-ferrite (with Fe/Mn ratio 10, diameter 14 nm) has been deposited on graphene oxide sheets (GO) which were grafted with oleylamine. After covalent attachment of mPEG₅₀₀₀-NH₂, the NPs with a hydrodynamic size of 82 nm had an r_2 value as high as $256 \text{ s}^{-1} \text{ mM}^{-1}$ (Fe at room temperature) [158]. A hybrid of GO (width: 50–500 nm, thickness: 0.8–1.1 nm) and MnFe₂O₄ spinels with a Fe/Mn ratio of about 2 showed a saturation magnetization (σ_s) close to 19.0 emu g^{-1} and $r_1 = 8.4$ and $r_2 = 81.3 \text{ s}^{-1} \text{ mM}^{-1}$ (Fe + Mn, 0.5 T, 36 °C). Thanks to the graphene oxide support this material also has strong optical absorbance in the near-infrared (NIR) region and good photothermal stability, which can be exploited for photothermal ablation of cancer cells. Furthermore, GO@MnFe₂O₄ nanohybrids loaded with doxorubicin have potential as theranostic in chemotherapy [159].

A tumor-targeting T_2 CA has been prepared by encapsulating 11.7 nm MnFe₂O₄ NPs into L- α -phosphatidylethanolamine-hyperbranched polyglycidol (PE-HBPG) bioconjugates covalently functionalized with folic acid (FA). The NPs had a σ_s of $59 \text{ A m}^2 \text{ kg}^{-1}$ and after the clustering they had an r_2 value of $141 \text{ s}^{-1} \text{ mM}^{-1}$ [68].

Attachment of 12 nm MnFe₂O₄ NPs to adenovirus resulted in hybrid systems, which are promising for in vivo MR tracking of targeted viral gene delivery therapies [56]. Fluorescent polyethylenimine cation-coated MnFe₂O₄ NPs (74 nm diameter) have been suggested for dual-mode human mesenchymal stem cell tracking [160]. The positively charged coated NPs are supposed to interact with the negatively charged cell surface and, in this way, to promote uptake of the NPs.

A different approach to contrast enhancement was taken by Choo et al., who encapsulated uniform octahedral MnFe₂O₄ NPs (diameter 18.4 nm) in polymeric nanospheres [161]. The superparamagnetic gel particles (hydrodynamic diameters 132–175 nm) showed separate ¹H resonances of the bulk water and water inside the gel particles with an induced shift difference that was 3.2 ppm irrespective of the amount of MnFe₂O₄ NPs inside the gel particles. This shift difference could be exploited for MRI at an offset frequency from the main water peak. In this way, the background interference by water was effectively eliminated and hence, the regions affected by the nanospheres would be exclusively detectable. The gel particles had also impressive r_2 values (191.9 – $632.6 \text{ s}^{-1} \text{ mM}^{-1}$ at 9.4 T, 298 K, depending on the hydrodynamic diameter and the loading with MnFe₂O₄).

Vamvakidis et al. constructed bi-magnetic clusters of the soft magnetic MnFe₂O₄ NPs (9 nm, $\sigma_s = 66 \text{ emu g}^{-1}$ and $H_C = 150 \text{ Oe}$ at 300 K) and the hard CoFe₂O₄ NPs (9 nm, $\sigma_s = 85 \text{ emu g}^{-1}$ and $H_C = 250 \text{ Oe}$ at 300 K), covered by sodium dodecyl sulfate [84]. A synergetic magnetic interaction of these species leads to clusters with a hydrodynamic diameter of 105 nm with both a high σ_s and H_C (90 emu g^{-1} and 250 Oe at 300 K, respectively). This makes these clusters promising for application as MRI CAs ($r_2 = 81.8 \text{ s}^{-1} \text{ mM}^{-1}$ at 1.5 T) and magnetic hyperthermic therapy. More recently, the same group encapsulated solvothermally prepared 9 nm MnFe₂O₄ NPs in grafted co-polymers endowed with multifunctional and responsive characteristics, such as thermo-responsive shrinking upon heating just above body temperature which has potential for drug delivery initiated by magnetic heating [71].

3.7. Manganese ferrites as T_1 MRI contrast agent

The longitudinal ¹H NMRD profiles reported for Mn_{1.1}Fe_{1.9}O₄ ($d = 3$ – 6 nm , see Fig. 15) exhibit a shape as predicted for a low anisotropy model (see Fig. 1) [125]. Only Mn-ferrite NPs with a high r_1/r_2 value are suitable for application as T_1 MRI CA. From Fig. 1 it can be concluded that for magnetic field strengths at which the currently most used clinical MRI scanners operate (0.5–1.5 T), a high σ_s and a small d ($<10 \text{ nm}$) are favorable to reach high r_1 values. This combination of requirements makes it necessary to avoid a large dead layer of the favorable ultra-small NPs by using a careful synthetic protocol. At the same time, the value of r_2 should be minimized, which also requires very small NPs but now with large dead and/or paramagnetic layers. Usually, the outer sphere mechanism is dominant, which implies that r_1 is proportional to σ_s (see Eq. (1)). It should be noted that the relative contribution of the inner sphere mechanism increases with a decrease in the diameter of NPs because of the increase of the number of paramagnetic atoms at the surface that are in direct contact with water protons relative to the inaccessible core atoms. Furthermore, coating with a compound rich in exchangeable protons may give rise to an additional large second sphere contribution.

The synthesis of small particles requires control of their composition and size. Using a co-precipitation procedure, this can be achieved by burst precipitation in the presence of multidentate polymeric ligands to avoid crystal growth. For example, Li et al. have prepared ultrasmall MnFe₂O₄ NPs by co-precipitation in the presence of poly(methacrylic acid) pentaerythritol tetrakis (3-mercapto propionate) [163]. The obtained NPs

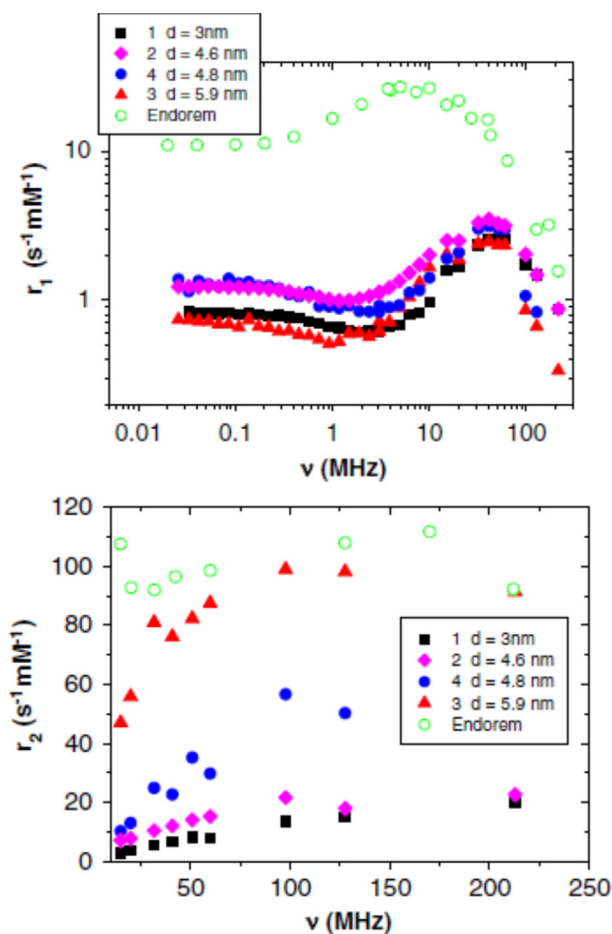


Fig. 15. Longitudinal and transverse ¹H NMRD profiles of Mn_{1.1}Fe_{1.9}O₄ NPs and the commercial superparamagnetic iron oxide CA “Endorem” at room temperature. Copied from Ref. [125] with permission. Copyright 2008, IOP Publishing Ltd.

in a range decreasing from 4.9 to 2.2 nm showed a decrease in σ_s from 11.6 to 0.22 A m² kg⁻¹ at 300 K. The smallest NPs had an almost linear σ -H curve, which suggests a very disordered structure that was almost exclusively paramagnetic of nature. XPS spectra indicated that Mn²⁺ was partially oxidized to Mn³⁺, which may have further reduced σ_s . All in all, it made this material a good r_1 CA ($r_1 = 6.61 \text{ s}^{-1} \text{ mM}^{-1}$, $r_2 = 35.92 \text{ s}^{-1} \text{ mM}^{-1}$ at 4.7 T and 300 K).

Thermal decomposition of metal complexes may be the preparation of choice. It is then important that the metal complexes exhibit simultaneous decomposition dynamics, which guarantees an initial burst of seeds with the correct stoichiometry. Zhang et al. have designed a procedure with a combination of Ferucitate (decomposition temperature 584 K) and Mn-oleate (decomposition temperature 599 K) that allowed the controlled synthesis of ultrasmall Mn-ferrite NPs with diameters of less than 4 nm [86]. With this procedure, MnFe₂O₄ NPs were prepared with diameters between 2 and 3.9 nm, which showed, after coating with phosphorylated mPEG₂₀₀₀, r_1 values between 8.43 and 6.98 at 3 T with r_2/r_1 ratios below 3.

Miao et al. have optimized 3 nm Mn_xFe_{3-x}O₄ NPs prepared by a solvothermal procedure [119]. The highest σ_s -values were obtained for NPs with a mPEG₁₀₀₀ coating for $x = 0.4$ – 0.8 , and the optimal r_1 ($10.35 \text{ s}^{-1} \text{ mM}^{-1}$ at 3 T; $r_2/r_1 = 2.29$) and ratio r_2/r_1 for $x = 0.75$. A series of samples of Mn_xFe_{3-x}O₄ NPs with different shapes (cubes, octapods, and plates) that were coated with citrate showed an increase in r_1 with an increase in x from 0 to 0.5. The σ_s -values for NPs with $x = 0.5$ having these shapes were 67.3, 64.8, and 40.5 A m² kg⁻¹, respectively [143]. The r_1 values of these NPs showed a similar trend (57.8, 62.1, and 22.4 s⁻¹ mM⁻¹, respectively at 0.5 T).

Ultrasmall MnFe₂O₄ NPs (diameter 3.9 nm) were coated with dihydrocinnamic acid and subsequently with the tumor-targeting peptide CREKA (cys-arg-glu-lys-ala) [118]. The resulting system had an r_1 value of 6.79 s⁻¹ mM⁻¹ at 7 T and 313 K. These NPs exhibited an enzyme-like response to the acidic and redox conditions in tumors by releasing Mn²⁺, which resulted in amplification of the contrast enhancement. In this way, a metastasis with a diameter of only 0.39 mm was detected.

3.8. Manganese ferrites as dual T_1 - T_2 MRI contrast agent

Quenching of longitudinal relaxation due to the high magnetization of Mn-ferrite NPs is a common problem. Choi et al. have tackled this by constructing core-shell particles separated by a silica layer [164]. The 15 nm core consisted of MnFe₂O₄ prepared by solvothermal decomposition of metal acetylacetonates, which served as a T_2 CA, whereas a thin outer layer (1.5 nm) of Gd³⁺-carbonate was used as a T_1 CA. Direct contact between water and the Gd³⁺ ions at the surface provided optimal longitudinal relaxation enhancement. The quenching of the r_1 by the magnetization of the core was minimized by tuning the thickness of the intermediate silica layer. Optimum values were obtained for MnFe₂O₄@-SiO₂@Gd₂O(CO₃)₂ NPs having a 16 nm thick SiO₂ layer, which were coated with poly(ethylene glycol) methyl ether methacrylate ($r_1 = 33.1 \text{ s}^{-1} \text{ mM}^{-1}$, $r_2 = 274 \text{ s}^{-1} \text{ mM}^{-1}$ at 4.7 T).

Another separation of the T_1 and T_2 enhancing functionalities was achieved with acorn like shaped Janus NPs MnFe₂O₄@MnO that were stabilized with PEG₄₀₀₀ [165]. The MnO side of these NPs has a relatively large amount of Mn²⁺ ions on its surface that boost the T_1 relaxation, whereas the MnFe₂O side provides a magnetization ($\sigma_s = 2.25 \text{ A m}^2 \text{ kg}^{-1}$ at room temperature) for enhancement of the T_2 relaxation. The ratio r_2/r_1 for these NPs was 10 at 1.41 T and room temperature.

The σ_s values of manganese ferrite NPs coated with gallol-PEG (MW = 3 kDa) have been shown to increase with the particle diam-

eter [81]. The longitudinal relaxivities appear to be almost independent of the size, whereas the transversal relaxivities strongly increased with the particle size. This allowed tuning these NPs through their size for application as dual T_1 - T_2 CA. Thanks to the PEG coating, these particles showed prolonged circulation times in vivo.

4. Conclusions

During the last two decades, much progress has been made in the understanding of the magnetic properties of Mn-ferrites. This allows the design of NPs with relaxivities tuned for optimal performance as MRI CAs. The Mn-ferrites are particularly efficient in enhancing the transverse relaxivities. The highest r_2 values can be obtained with Mn_{0.6}Zn_{0.4}Fe₂O₄ and Mn_{0.4}Fe_{2.6}O₄ NPs with diameters of about 20 nm. A minimal magnetically dead layer is necessary to reach maximal relaxivities, which seems to be achievable by a carefully performed solvothermal synthesis eventually followed by a seed growth procedure. The as-synthesized NPs are hydrophobic and consequently, they need to be made water-dispersible by covering with a hydrophilic coating for application as MRI CAs. Minimal thickness of the coating generally is favorable to achieve high relaxivities. NPs of less than 20 nm are generally in the MAR. The highest r_2 values are obtained near the border with the SDR. In principle, higher r_2 -values would be possible by clustering to NPs with larger diameters but then passing the border of SDR and PRR should be avoided if T_2 CAs are needed because then r_2 -values decrease with increasing diameter in the PRR, whereas r_2^* remains constant. The magnetization of these systems generally are saturated at magnetic field strengths higher than about 0.5 T, and consequently, the r_2 values are then independent of the magnetic field strength r_2 . Values up to about 600–800 s⁻¹ mM⁻¹ at room temperature can be reached. The r_2 values are higher than those reported for commercial iron oxide NPs, which exhibit $r_2 < 120 \text{ s}^{-1} \text{ mM}^{-1}$ [18].

The transverse relaxation of Mn-ferrites is generally much faster than the longitudinal relaxation, which may lead to signal loss in T_1 -weighted MRI. This effect becomes more serious upon an increase of the magnetic field strength because the longitudinal relaxation rates decrease significantly upon an increase of the magnetic field strength, whereas the transverse relaxation rates are about constant above 0.5–1 T. Sufficiently low ratios r_2/r_1 for application as MRI T_1 CAs are only possible with ultrasmall NPs (<10 nm). With those systems, r_1 values up to about 60 have been reported.

Many factors other than relaxivity determine whether a particular nanoparticulate material is suitable as an MRI CA, including its biodistribution and toxicity [166], which are both dependent on the size of the NPs and the nature of the coatings. Many publications in this field report on pre-clinical tests, such as cytotoxicity tests and studies on various cell lines. Many in vivo studies have been reported mainly on mice, sometimes with implanted tumors. These are not discussed in detail as this review focuses on the relaxivity characteristics of these agents. To the best of my knowledge, no clinical studies on humans have been performed with these agents. At present, the extremely high costs of clinical trials of MRI CAs are a major obstacle to the introduction of new agents, especially as the expected market of these agents is small compared to that of more profitable blockbuster pharmaceuticals applied for wide-spread chronic diseases [6]. However, due to the trend toward personalized medicine, there is an increasing interest in new theranostics. The manganese ferrites are very promising in this regard, because they can act as efficient agents for magnetic hyperthermic therapy as well as diagnostic agents.

Declaration of Competing Interest

The author declares that he has no known competing financial interests or personal relationships that could have appeared to influence the work reported in this paper.

Acknowledgment

I am grateful to Dr. Kristina Djanashvili for her helpful comments on this manuscript.

Funding

This research did not receive any specific grant from funding agencies in the public, commercial, or not-for-profit sectors.

References

- P.C. Lauterbur, Image Formation by Induced local interactions: examples employing nuclear magnetic resonance, *Nature* 242 (1973) 190–191, <https://doi.org/10.1038/242190a0>.
- J. Lohrke, T. Frenzel, J. Endrikat, F.C. Alves, T.M. Grist, M. Law, J.M. Lee, T. Leiner, K.-C. Li, K. Nikolaou, M.R. Prince, M.R. Prince, H.H. Schild, J.C. Weinreb, K. Yoshikawa, H. Pietsch, 25 Years of contrast-enhanced MRI: Developments, current challenges and future perspectives, *Adv. Ther.* 33 (2016) 1–28, <https://doi.org/10.1007/s12325-015-0275-4>.
- Merbach A.E., Helm L., Tóth É., The chemistry of contrast agents in medical magnetic resonance imaging, second ed., John Wiley & Sons, Ltd, Chichester (UK, 2013, <https://doi.org/10.1002/9781118503652>.
- P. Caravan, J.J. Ellison, T.J. McMurry, R.B. Lauffer, Gadolinium(III) chelates as MRI contrast agents: structure, dynamics, and applications, *Chem. Rev.* 99 (1999) 2293–2352, <https://doi.org/10.1021/cr980440x>.
- V.C. Pierre, M.J. Allen, P. Caravan, Contrast agents for MRI: 30+ years and where are we going?, *J. Biol. Inorg. Chem.* 19 (2014) 127–131, <https://doi.org/10.1007/s00775-013-1074-5>.
- J. Wahsner, E.M. Gale, A. Rodríguez-Rodríguez, P. Caravan, Chemistry of MRI contrast agents: current challenges and new frontiers, *Chem. Rev.* 119 (2019) 957–1057, <https://doi.org/10.1021/acs.chemrev.8b00363>.
- A.G. Bleicher, E. Kanal, Assessment of adverse reaction rates to a newly approved MRI contrast agent: review of 23,553 administrations of gadobenate dimeglumine, *Am. J. Roentgenol.* 191 (2008) W307–W311, <https://doi.org/10.2214/AJR.07.3951>.
- E. Kanal, M.F. Tweedle, Residual or retained gadolinium: practical implications for radiologists and our patients, *Radiology* 275 (2015) 630–634, <https://doi.org/10.1148/radiol.2015150805>.
- Z. Baranyai, E. Brücher, F. Uggeri, A. Maiocchi, I. Tóth, M. András, A. Gáspár, L. Zékány, S. Aime, The role of equilibrium and kinetic properties in the dissociation of Gd[DTPA-bis(methylamide)] (Omniscan) at near to physiological conditions, *Chem. Eur. J.* 21 (2015) 4789–4799, <https://doi.org/10.1002/chem.201405967>.
- E. Brücher, G. Tircsó, Z. Baranyai, Z. Kovács, A.D. Sherry, Stability and toxicity of contrast agents, in: A.E. Merbach, L. Helm, É. Tóth (Eds.), *The Chemistry of Contrast Agents in Medical Magnetic Resonance Imaging*, John Wiley & Sons Ltd., Chichester (UK), 2013, pp. 157–208, <https://doi.org/10.1002/9781118503652.ch4>.
- T. Kanda, T. Fukusato, M. Matsuda, K. Toyoda, H. Oba, J.I. Kotoku, T. Haruyama, K. Kitajima, S. Furui, Gadolinium-based contrast agent accumulates in the brain even in subjects without severe renal dysfunction: evaluation of autopsy brain specimens with inductively coupled plasma mass spectroscopy, *Radiology* 276 (2015) 228–232, <https://doi.org/10.1148/radiol.2015142690>.
- R. Pullicino, M. Radon, S. Biswas, M. Bhojak, K. Das, A review of the current evidence on gadolinium deposition in the brain, *Clin. Neuroradiol.* 28 (2018) 159–169, <https://doi.org/10.1007/s00062-018-0678-0>.
- P. Robert, X. Violas, S. Grand, S. Lehericy, J.-M. Idee, S. Ballet, C. Corot, Linear gadolinium-based contrast agents are associated with brain gadolinium retention in healthy rats, *Invest. Radiol.* 51 (2016) 73–82, <https://doi.org/10.1097/RLI.0000000000000241>.
- N.M.D. Murata, L.F. Gonzalez-Cuyar, K. Murata, C. Fligner, R. Dills, D. Hippe, K. R. Maravilla, Macrocyclic and other non-group 1 gadolinium contrast agents deposit low levels of gadolinium in brain and bone tissue: preliminary results from 9 patients with normal renal function, *Invest. Radiol.* 51 (2016) 447–453, <https://doi.org/10.1097/RLI.0000000000000252>.
- A. Splendiani, M. Perri, C. Marsecano, V. Vellucci, G. Michelini, A. Barile, E. Di Cesare, Effects of serial macrocyclic-based contrast materials gadoterate meglumine and gadobutrol administrations on gadolinium-related dentate nuclei signal increases in enhanced T₁-weighted brain: a retrospective study in 158 multiple sclerosis (MS) patients, *Radiol. Med.* 123 (2018) 125–134, <https://doi.org/10.1007/s11547-017-0816-9>.
- M. Botta, F. Carniato, D. Esteban-Gómez, C. Platas-Iglesias, L. Tei, Mn(II) compounds as an alternative to Gd-based MRI probes, *Future Med. Chem.* 11 (2019) 1461–1483, <https://doi.org/10.4155/fmc-2018-0608>.
- CRC Handbook of Chemistry and Physics, 2016–2017.
- S. Laurent, D. Forge, M. Port, A. Roch, C. Robic, L. Vander Elst, R.N. Muller, Magnetic iron oxide nanoparticles: synthesis, stabilization, vectorization, physicochemical characterizations, and biological applications, *Chem. Rev.* 108 (2008) 2064–2110, <https://doi.org/10.1021/cr068445e>.
- P.A. Rinck, MR imaging: quo vadis?, *Rinckside* 30 (2019) 5–8 <http://rinckside.org/Rinckside%20Columns/2019%2003%2020MRI%2020quo%2020vadis.htm>.
- P.A. Rinck, Magnetic resonance in medicine; a critical introduction, BoD, Hamburg, Germany, 2020.
- O. Karovic, I. Tonazzini, N. Rebola, E. Edström, C. Lövdahl, B.B. Fredholm, E. Daré, Toxic effects of cobalt in primary cultures of mouse astrocytes: Similarities with hypoxia and role of HIF-1 α , *Biochem. Pharmacol.* 73 (2007) 694–708, <https://doi.org/10.1016/j.bcp.2006.11.008>.
- Y.-M. Kwon, Z. Xia, S. Glyn-Jones, D. Beard, H.S. Gill, D.W. Murray, Dose-dependent cytotoxicity of clinically relevant cobalt nanoparticles and ions on macrophages in vitro, *Biomed. Mater.* 4 (2009) 025018, <https://doi.org/10.1088/1748-6041/4/2/025018>.
- F. Ahmad, H. Yao, Y. Zhou, X. Liu, Toxicity of cobalt ferrite (CoFe₂O₄) nanobeads in *Chlorella vulgaris*: Interaction, adaptation and oxidative stress, *Chemosphere* 139 (2015) 479–485, <https://doi.org/10.1016/j.chemosphere.2015.08.008>.
- S.Z. Mirahmadi-Zare, A. Allafchian, F. Aboutalebi, P. Shojaei, Y. Khazaie, K. Dormiani, L. Lachinani, M.-H. Nasr-Esfahani, Super magnetic nanoparticles NiFe₂O₄, coated with aluminum–nickel oxide sol-gel lattices to safe, sensitive and selective purification of his-tagged proteins, *Protein Expression Purif.* 121 (2016) 52–60, <https://doi.org/10.1016/j.pep.2016.01.008>.
- Q.L. Vuong, P. Gillis, A. Roch, Y. Gossuin, Magnetic resonance relaxation induced by superparamagnetic particles used as contrast agents in magnetic resonance imaging: a theoretical review, *Wiley Interdiscip. Rev.: Nanomed. Nanobiotechnol.* 9 (2017) e1468, <https://doi.org/10.1002/wnan.1468>.
- É. Tóth, L. Helm, A.E. Merbach, Relaxivity of gadolinium(III) complexes: theory and mechanism, in: É. Tóth, L. Helm, A.E. Merbach (Eds.), *Chemistry of Contrast Agents in Medical Magnetic Resonance Imaging*, John Wiley & Sons Ltd., Chichester U.K., 2013, pp. 25–81, <https://doi.org/10.1002/9781118503652.ch2>.
- A. Roch, R.N. Muller, P. Gillis, Theory of proton relaxation induced by superparamagnetic particles, *J. Chem. Phys.* 110 (1999) 5403–5411, <https://doi.org/10.1063/1.478435>.
- M. Lévy, F. Gazeau, C. Wilhelm, S. Neveu, M. Devaud, P. Levitz, Revisiting MRI contrast properties of nanoparticles: beyond the superparamagnetic regime, *J. Phys. Chem. C* 117 (2013) 15369–15374, <https://doi.org/10.1021/jp404199f>.
- H.W. de Haan, Mechanisms of proton spin dephasing in a system of magnetic particles, *Magn. Reson. Med.* 66 (2011) 1748–1758, <https://doi.org/10.1002/mrm.22966>.
- Q.L. Vuong, J.-F. Berret, J. Fresnais, Y. Gossuin, O. Sandre, A universal scaling law to predict the efficiency of magnetic nanoparticles as MRI T₂-contrast agents, *Adv. Healthcare Mater.* 1 (2012) 502–512, <https://doi.org/10.1002/adhm.201200078>.
- Q.L. Vuong, Y. Gossuin, P. Gillis, S. Delangre, New simulation approach using classical formalism to water nuclear magnetic relaxation dispersions in presence of superparamagnetic particles used as MRI contrast agents, *J. Chem. Phys.* 137 (2012), 114505, <https://doi.org/10.1063/1.4751442>.
- Y. Gossuin, T. Orlando, M. Basini, D. Henrard, A. Lascialfari, C. Mattea, S. Stapf, Q.L. Vuong, NMR relaxation induced by iron oxide particles: testing theoretical models, *Nanotechnology* 27 (2016), 155706, <https://doi.org/10.1088/0957-4484/27/15/155706>.
- R.A. Brooks, F. Moiny, P. Gillis, On T₂-shortening by weakly magnetized particles: the chemical exchange model, *Magn. Reson. Med.* 45 (2001) 1014–1020, <https://doi.org/10.1002/mrm.1135>.
- R.J.S. Brown, Distribution of fields from randomly placed dipoles: free-precession signal decay as result of magnetic grains, *Phys. Rev.* 121 (1961) 1379–1382, <https://doi.org/10.1103/PhysRev.121.1379>.
- D.A. Yablonskiy, E.M. Haacke, Theory of NMR signal behavior in magnetically inhomogeneous tissues: the static dephasing regime, *Magn. Reson. Med.* 32 (1994) 749–763, <https://doi.org/10.1002/mrm.1910320610>.
- P. Gillis, F. Moiny, R.A. Brooks, On T₂-shortening by strongly magnetized spheres: a partial refocusing model, *Magn. Reson. Med.* 47 (2002) 257–263, <https://doi.org/10.1002/mrm.10059>.
- A. Roch, Y. Gossuin, R.N. Muller, P. Gillis, Superparamagnetic colloid suspensions: water magnetic relaxation and clustering, *J. Magn. Magn. Mater.* 293 (2005) 532–539, <https://doi.org/10.1016/j.jmmm.2005.01.070>.
- F.T. Kurz, T. Kampf, S. Heiland, M. Bendszus, H.-P. Schlemmer, C.H. Ziener, Theoretical model of the single spin-echo relaxation time for spherical magnetic perturbers, *Magn. Reson. Med.* 71 (2014) 1888–1895, <https://doi.org/10.1002/mrm.25196>.
- S.L.C. Pinho, G.A. Pereira, P. Voisin, J. Kassem, V. Bouchaud, L. Etienne, J.A. Peters, L. Carlos, S. Mornet, C.F.G.C. Geraldes, J. Rocha, M.-H. Delville, Fine tuning of the relaxometry of γ -Fe₂O₃@SiO₂ nanoparticles by tweaking the silica coating thickness, *ACS Nano* 4 (2010) 5339–5349, <https://doi.org/10.1021/nn101129r>.

- [40] D.-X. Chen, N. Sun, H.-C. Gu, Size analysis of carboxydextran coated superparamagnetic iron oxide particles used as contrast agents of magnetic resonance imaging, *J. Appl. Phys.* 106 (2009) 063906, <https://doi.org/10.1063/1.3211307>.
- [41] H.W. de Haan, C. Paquet, Enhancement and degradation of the R^{2*} relaxation rate resulting from the encapsulation of magnetic particles with hydrophilic coatings, *Magn. Reson. Med.* 66 (2011) 1759–1766, <https://doi.org/10.1002/mrm.22944>.
- [42] K. Vamvakidis, M. Katsikini, D. Sakellari, E.C. Paloura, O. Kalogirou, C. Dendrinou-Samara, Reducing the inversion degree of $MnFe_2O_4$ nanoparticles through synthesis to enhance magnetization: evaluation of their 1H NMR relaxation and heating efficiency, *Dalton Trans.* 43 (2014) 12754–12765, <https://doi.org/10.1039/c4dt00162a>.
- [43] A.A. v.d. Giessen, Magnetic properties of ultra-fine iron (III) oxide-hydrate particles prepared from iron (III) oxide-hydrate gels, *J. Phys. Chem. Solids* 28 (1967) 343–346, [https://doi.org/10.1016/0022-3697\(67\)90130-8](https://doi.org/10.1016/0022-3697(67)90130-8).
- [44] R.E. Rosensweig, Heating magnetic fluid with alternating magnetic field, *J. Magn. Magn. Mater.* 252 (2002) 370–374, [https://doi.org/10.1016/S0304-8853\(02\)00706-0](https://doi.org/10.1016/S0304-8853(02)00706-0).
- [45] M.B. Bannwarth, S. Ebert, M. Lauck, U. Ziener, S. Tomcin, G. Jakob, K. Muennemann, V. Mailaender, A. Musyanovych, K. Landfester, Tailor-made nanocapsules for combined magnetic-field-induced release and MRI, *Macromol. Biosci.* 14 (2014) 1205–1214, <https://doi.org/10.1002/mabi.201400122>.
- [46] Cullity B.D., Graham C.D., *Ferrimagnetism, Introduction to magnetic materials*, Wiley-IEEE Press, 2009, pp. 175–195, <https://doi.org/10.1002/9780470386323.ch6>.
- [47] J. Smit, H.P.J. Wijn, *Ferrites*, Philips' Technical Library, 1959.
- [48] E.J.W. Verwey, E.L. Heilmann, Physical properties and cation arrangement of oxides with spinel structures I. Cation arrangement in spinels, *J. Chem. Phys.* 15 (1947) 174–180, <https://doi.org/10.1063/1.1746464>.
- [49] R.J. Hill, J.R. Craig, G.V. Gibbs, Systematics of the spinel structure type, *Phys. Chem. Miner.* 4 (1979) 317–339, <https://doi.org/10.1007/bf00307535>.
- [50] W.S. Galvão, D.M.A. Neto, R.M. Freire, P.B.A. Fechine, Super-paramagnetic nanoparticles with spinel structure: a review of synthesis and biomedical applications, *Solid State Phenom.* 241 (2016) 139–176, <https://doi.org/10.4028/www.scientific.net/SSP.241.139>.
- [51] J.M. Hastings, L.M. Corliss, Neutron diffraction study of manganese ferrite, *Phys. Rev.* 104 (1956) 328–331, <https://doi.org/10.1103/PhysRev.104.328>.
- [52] V. Chlan, V. Procházková, H. Štěpánková, B. Sedláčková, P. Novák, Z. Šimša, V.A.M. Brabers, ^{57}Fe NMR study of manganese ferrites, *J. Magn. Magn. Mater.* 320 (2008) e96–e99, <https://doi.org/10.1016/j.jmmm.2008.02.022>.
- [53] J.-H. Lee, Y.-M. Huh, Y.-W. Jun, J.-W. Seo, J.-T. Jang, H.-T. Song, S. Kim, E.-J. Cho, H.-G. Yoon, J.-S. Suh, J. Cheon, Artificially engineered magnetic nanoparticles for ultra-sensitive molecular imaging, *Nat. Med.* 13 (2007) 95–99, <https://doi.org/10.1038/nm1467>.
- [54] P.J. van der Zaag, A. Noordermeer, M.T. Johnson, P.F. Bongers, Comment on “Size-dependent Curie temperature in nanoscale $MnFe_2O_4$ particles”, *Phys. Rev. Lett.* 68 (1992) 3112, <https://doi.org/10.1103/PhysRevLett.68.3112>.
- [55] A. Broese van Groenou, P.F. Bongers, A.L. Stuyts, Magnetism, microstructure and crystal chemistry of spinel ferrites, *Mater. Sci. Eng. 3* (1969) 317–392, [https://doi.org/10.1016/0025-5416\(69\)90042-1](https://doi.org/10.1016/0025-5416(69)90042-1).
- [56] Y.M. Huh, E.S. Lee, J.H. Lee, Y.W. Jun, P.H. Kim, C.O. Yun, J.H. Kim, J.S. Suh, J. Cheon, Hybrid nanoparticles for magnetic resonance imaging of target-specific viral gene delivery, *Adv. Mater.* 19 (2007) 3109–3112, <https://doi.org/10.1002/adma.200701952>.
- [57] Y.-W. Jun, J.-H. Lee, J. Cheon, Chemical design of nanoparticle probes for high-performance magnetic resonance imaging, *Angew. Chem., Int. Ed.* 47 (2008) 5122–5135, <https://doi.org/10.1002/anie.200701674>.
- [58] Y.-W. Jun, J.-W. Seo, J. Cheon, Nanoscaling laws of magnetic nanoparticles and their applicabilities in biomedical sciences, *Acc. Chem. Res.* 41 (2008) 179–189, <https://doi.org/10.1021/ar700121f>.
- [59] J.W.M. Bulte, R.A. Brooks, B.M. Moskowitz, H.L. Bryant Jr., J.A. Frank, Relaxometry, magnetometry, and EPR evidence for three magnetic phases in the MR contrast agent MION-46L, *J. Magn. Magn. Mater.* 194 (1999) 217–223, [https://doi.org/10.1016/S0304-8853\(98\)00555-1](https://doi.org/10.1016/S0304-8853(98)00555-1).
- [60] C. Pereira, A.M. Pereira, C. Fernandes, M. Rocha, R. Mendes, M.P. Fernández-García, A. Guedes, P.B. Tavares, J.-M. Grenèche, J.P. Araújo, C. Freire, Superparamagnetic MFe_2O_4 ($M = Fe, Co, Mn$) nanoparticles: tuning the particle size and magnetic properties through a novel one-step coprecipitation route, *Chem. Mater.* 24 (2012) 1496–1504, <https://doi.org/10.1021/cm300301c>.
- [61] A. Millan, A. Urtizberea, N.J.O. Silva, F. Palacio, V.S. Amaral, E. Snoeck, V. Serin, Surface effects in maghemite nanoparticles, *J. Magn. Magn. Mater.* 312 (2007) L5–L9, <https://doi.org/10.1016/j.jmmm.2006.09.011>.
- [62] X. Batlle, Finite-size effects in fine particles: magnetic and transport properties, *J. Phys. D: Appl. Phys.* 35 (2002) 15, <https://doi.org/10.1088/0022-3727/35/6/201>.
- [63] J.P. Chen, C.M. Sorensen, K.J. Klabunde, G.C. Hadjipanayis, E. Devlin, A. Kostikas, Size-dependent magnetic properties of $MnFe_2O_4$ fine particles synthesized by coprecipitation, *Phys. Rev. B* 54 (1996) 9288–9296, <https://doi.org/10.1103/PhysRevB.54.9288>.
- [64] B. Aslibeiki, P. Kameli, M.H. Ehsani, $MnFe_2O_4$ bulk, nanoparticles and film: A comparative study of structural and magnetic properties, *Ceram. Int.* 42 (2016) 12789–12795, <https://doi.org/10.1016/j.ceramint.2016.05.041>.
- [65] Z.X. Tang, C.M. Sorensen, K.J. Klabunde, G.C. Hadjipanayis, Size-dependent Curie temperature in nanoscale $MnFe_2O_4$ particles, *Phys. Rev. Lett.* 67 (1991) 3602–3605.
- [66] A. Banerjee, B. Blasiak, E. Pasquier, B. Tomanek, S. Trudel, Synthesis, characterization, and evaluation of PEGylated first-row transition metal ferrite nanoparticles as T_2 contrast agents for high-field MRI, *RSC Adv.* 7 (2017) 38125–38134, <https://doi.org/10.1039/C7RA05495E>.
- [67] The reported plots were digitized with: WebPlotDigitizer, <https://automeris.io/WebPlotDigitizer/> (last accessed: 30-06-2020).
- [68] R. Augustine, H.R. Lee, H. Kim, Y. Zhang, I. Kim, Hyperbranched lipopolymer-folate-stabilized manganese ferrite nanoparticles for the water-soluble targeted MRI contrast agent, *React. Funct. Polym.* 144 (2019) 104352, <https://doi.org/10.1016/j.reactfunctpolym.2019.104352>.
- [69] Y. Du, X. Liu, Q. Liang, X.-J. Liang, J. Tian, Optimization and design of magnetic ferrite nanoparticles with uniform tumor distribution for highly sensitive MRI/MPI Performance and improved magnetic hyperthermia therapy, *Nano Lett.* 19 (2019) 3618–3626, <https://doi.org/10.1021/acs.nanolett.9b00630>.
- [70] M. Günay, H. Erdem, A. Baykal, H. Sözeri, M.S. Toprak, Triethylene glycol stabilized $MnFe_2O_4$ nanoparticle: synthesis, magnetic and electrical characterization, *Mater. Res. Bull.* 48 (2013) 1057–1064, <https://doi.org/10.1016/j.materresbull.2012.11.097>.
- [71] Z. Iatridi, K. Vamvakidis, I. Tsougos, K. Vassiou, C. Dendrinou-Samara, G. Bokias, Multifunctional polymeric platform of magnetic ferrite colloidal superparticles for luminescence, imaging, and hyperthermia applications, *ACS Appl. Mater. Interfaces* 8 (2016) 35059–35070, <https://doi.org/10.1021/acsmi.6b13161>.
- [72] D. Kim, Y.T. Thai, D.E. Nikles, C.S. Brazel, Heating of aqueous dispersions containing $MnFe_2O_4$ nanoparticles by radio-frequency magnetic field induction, *IEEE Trans. Magn.* 45 (2009) 64–70, <https://doi.org/10.1109/TMAG.2008.2005329>.
- [73] S. Kumar, A. Daverey, V. Khalilzad-Sharghi, N.K. Sahu, S. Kidambi, S.F. Othman, D. Bahadur, Theranostic fluorescent silica encapsulated magnetic nanoassemblies for in vitro MRI imaging and hyperthermia, *RSC Adv.* 5 (2015) 53180–53188, <https://doi.org/10.1039/C5RA07632C>.
- [74] E.-K. Lim, J. Yang, J.-S. Suh, Y.-M. Huh, S. Haam, Self-labeled magneto nanoprobes using tri-aminated polysorbate 80 for detection of human mesenchymal stem cells, *J. Mater. Chem.* 19 (2009) 8958–8963, <https://doi.org/10.1039/B912149H>.
- [75] J. Lu, S. Ma, J. Sun, C. Xia, C. Liu, Z. Wang, X. Zhao, F. Gao, Q. Gong, B. Song, X. Shuai, H. Ai, Z. Gu, Manganese ferrite nanoparticle micellar nanocomposites as MRI contrast agent for liver imaging, *Biomaterials* 30 (2009) 2919–2928, <https://doi.org/10.1016/j.biomaterials.2009.02.001>.
- [76] E. Mazarío, J. Sánchez-Marcos, N. Menéndez, M. Cañete, A. Mayoral, S. Rivera-Fernández, J.M. de la Fuente, P. Herrasti, High specific absorption rate and transverse relaxivity effects in manganese ferrite nanoparticles obtained by an electrochemical route, *J. Phys. Chem. C* 119 (2015) 6828–6834, <https://doi.org/10.1021/jp510937r>.
- [77] M. Menelaou, Z. Iatridi, I. Tsougos, K. Vasiou, C. Dendrinou-Samara, G. Bokias, Magnetic colloidal superparticles of Co, Mn and Ni ferrite featured with comb-type and/or linear amphiphilic polyelectrolytes, NMR and MRI relaxometry, *Dalton Trans.* 44 (2015) 10980–10990, <https://doi.org/10.1039/C5DT00372E>.
- [78] J. Mohapatra, A. Mitra, D. Bahadur, M. Aslam, Surface controlled synthesis of MFe_2O_4 ($M = Mn, Fe, Co, Ni$ and Zn) nanoparticles and their magnetic characteristics, *CrystEngComm* 15 (2013) 524–532, <https://doi.org/10.1039/C2CE25957E>.
- [79] V. Nandwana, S.-R. Ryoo, S. Kanthala, M. De, S.S. Chou, P.V. Prasad, V.P. Dravid, Engineered theranostic magnetic nanostructures: role of composition and surface coating on magnetic resonance imaging contrast and thermal activation, *ACS Appl. Mater. Interfaces* 8 (2016) 6953–6961, <https://doi.org/10.1021/acsmi.6b01377>.
- [80] J. Park, B. Kang, B. Kim, J.-S. Suh, Y.-M. Huh, S. Haam, A systematic study of core size and coating thickness on manganese-doped nanocrystals for high T_2 relaxivity as magnetic resonance contrast agent, *Nano Converg.* 2 (2015) 3/1–3/8, <https://doi.org/10.1186/s40580-014-0032-4>.
- [81] M. Pernía Leal, S. Rivera-Fernández, J.M. Franco, D. Pozo, J.M. de la Fuente, M. L. García-Martin, Long-circulating PEGylated manganese ferrite nanoparticles for MRI-based molecular imaging, *Nanoscale* 7 (2015) 2050–2059, <https://doi.org/10.1039/C4NR05781C>.
- [82] M. Ravichandran, S. Velumani, Manganese ferrite nanocubes as an MRI contrast agent, *Mater. Res. Express* 7 (2020) 16107, <https://doi.org/10.1088/2053-1591/ab66a4>.
- [83] N. Venkatesha, S.M. Pudukalakatti, Y. Qurishi, H.S. Atreya, C. Srivastava, $MnFe_2O_4$ - Fe_3O_4 core-shell nanoparticles as a potential contrast agent for magnetic resonance imaging, *RSC Adv.* 5 (2015) 97807–97815, <https://doi.org/10.1039/C5RA20474G>.
- [84] K. Vamvakidis, S. Mourdikoudis, A. Makridis, E. Paulidou, M. Angelakeris, C. Dendrinou-Samara, Magnetic hyperthermia efficiency and MRI contrast sensitivity of colloidal soft/hard ferrite nanoclusters, *J. Colloid Interface Sci.* 511 (2018) 101–109, <https://doi.org/10.1016/j.jcis.2017.10.001>.
- [85] H. Yang, C. Zhang, X. Shi, H. Hu, X. Du, Y. Fang, Y. Ma, H. Wu, S. Yang, Water-soluble superparamagnetic manganese ferrite nanoparticles for magnetic resonance imaging, *Biomaterials* 31 (2010) 3667–3673, <https://doi.org/10.1016/j.biomaterials.2010.01.055>.

- [86] H. Zhang, L. Li, X.L. Liu, J. Jiao, C.-T. Ng, J.B. Yi, Y.E. Luo, B.-H. Bay, L.Y. Zhao, M.L. Peng, N. Gu, H.M. Fan, Ultrasmall ferrite nanoparticles synthesized via dynamic simultaneous thermal decomposition for high-performance and multifunctional T₁ magnetic resonance imaging contrast agent, *ACS Nano* 11 (2017) 3614–3631, <https://doi.org/10.1021/acsnano.6b07684>.
- [87] J.-T. Jang, H. Nah, J.-H. Lee, S.H. Moon, M.G. Kim, J. Cheon, Critical enhancements of MRI contrast and hyperthermic effects by dopant-controlled magnetic nanoparticles, *Angew. Chem., Int. Ed.* 48 (2009) 1234–1238, <https://doi.org/10.1002/anie.200805149>.
- [88] M. Gaumet, A. Vargas, R. Gurny, F. Delie, Nanoparticles for drug delivery: The need for precision in reporting particle size parameters, *Eur. J. Pharm. Biopharm.* 69 (2008) 1–9, <https://doi.org/10.1016/j.ejpb.2007.08.001>.
- [89] B.D. Chithrani, W.C.W. Chan, Elucidating the mechanism of cellular uptake and removal of protein-coated gold nanoparticles of different sizes and shapes, *Nano Lett.* 7 (2007) 1542–1550, <https://doi.org/10.1021/nl070363y>.
- [90] H. Lee, T.-J. Yoon, J.-L. Figueiredo, F.K. Swirski, R. Weissleder, Rapid detection and profiling of cancer cells in fine-needle aspirates, *Proc. Natl. Acad. Sci. U. S. A.* 106 (2009) 12459–12464, <https://doi.org/10.1073/pnas.0902365106>.
- [91] G. Kandasamy, Recent advancements in manganite perovskites and spinel ferrite-based magnetic nanoparticles for biomedical theranostic applications, *Nanotechnology* 30 (2019) 502001, <https://doi.org/10.1088/1361-6528/ab3f17>.
- [92] O.F. Odio, E. Reguera, Nanostructured spinel ferrites: synthesis, functionalization, nanomagnetism and environmental applications, in: M.S. Seehra (Ed.) *Magnetic spinels*, IntechOpen, London, 2017, 10.5772/67513.
- [93] S. Sun, H. Zeng, D.B. Robinson, S. Raoux, P.M. Rice, S.X. Wang, G. Li, Monodisperse MFe₂O₄ (M = Fe, Co, Mn) nanoparticles, *J. Am. Chem. Soc.* 126 (2004) 273–279, <https://doi.org/10.1021/ja0380852>.
- [94] A.-H. Lu, E.L. Salabas, F. Schüth, Magnetic nanoparticles: synthesis, protection, functionalization, and application, *Angew. Chem., Int. Ed.* 46 (2007) 1222–1244, <https://doi.org/10.1002/anie.200602866>.
- [95] A. Yang, C.N. Chinnaamy, J.M. Greneche, Y. Chen, S.D. Yoon, Z. Chen, K. Hsu, Z. Cai, K. Ziemer, C. Vittoria, V.G. Harris, Enhanced Néel temperature in Mn ferrite nanoparticles linked to growth-rate-induced cation inversion, *Nanotechnology* 20 (2009), 185704, <https://doi.org/10.1088/0957-4484/20/18/185704>.
- [96] D. Levy, L. Pastero, A. Hoser, G. Viscovo, Thermal expansion and cation partitioning of MnFe₂O₄ (Jacobite) from 1.6 to 1276 K studied by using neutron powder diffraction, *Solid State Commun.* 201 (2015) 15–19, <https://doi.org/10.1016/j.ssc.2014.10.001>.
- [97] Z. Jiráček, S. Vratislav, Temperature dependence of distribution of cations in MnFe₂O₄, *Czech. J. Phys. B* 24 (1974) 642–647, <https://doi.org/10.1007/bf01587300>.
- [98] Z.J. Zhang, Z.L. Wang, B.C. Chakoumakos, J.S. Yin, Temperature dependence of cation distribution and oxidation state in magnetic Mn–Fe ferrite nanocrystals, *J. Am. Chem. Soc.* 120 (1998) 1800–1804, <https://doi.org/10.1021/ja9730851>.
- [99] D. Carta, M.F. Casula, P. Floris, A. Falqui, G. Mountjoy, A. Boni, C. Sangregorio, A. Corrias, Synthesis and microstructure of manganese ferrite colloidal nanocrystals, *Phys. Chem. Chem. Phys.* 12 (2010) 5074–5083, <https://doi.org/10.1039/B922646j>.
- [100] G. Davies, L.J. Kirschenbaum, K. Kustin, Kinetics and stoichiometry of the reaction between manganese(III) and hydrogen peroxide in acid perchlorate solution, *Inorg. Chem.* 7 (1968) 146–154, <https://doi.org/10.1021/ic50059a031>.
- [101] P. Veverka, O. Kaman, M. Kačénka, V. Herynek, M. Veverka, E. Šantavá, I. Lukeš, Z. Jiráček, Magnetic La_{1-x}Sr_xMnO₃ nanoparticles as contrast agents for MRI: the parameters affecting ¹H transverse relaxation, *J. Nanopart. Res.* 17 (2015) 33, <https://doi.org/10.1007/s11051-014-2848-6>.
- [102] O. Kaman, T. Dědourková, J. Koptan, J. Kuličková, M. Maryško, P. Veverka, R. Havelek, K. Královce, K. Turnovcová, P. Jendelová, A. Schröfel, L. Svoboda, Silica-coated manganite and Mn-based ferrite nanoparticles: a comparative study focused on cytotoxicity, *J. Nanopart. Res.* 18 (2016) 100, <https://doi.org/10.1007/s11051-016-3402-5>.
- [103] T.N. Stokes, G.D. Bromiley, G.D. Gatta, N. Rotiroti, N.J. Potts, K. Saunders, Cation distribution and valence in synthetic Al-Mn-O and Fe-Mn-O spinels under varying f_{o2} conditions, *Mineral. Mag.* 82 (2018) 975–992, <https://doi.org/10.1180/mgm.2018.109>.
- [104] M. Rotter, B. Sedláček, Z. Šimša, V.A.M. Brabers, NMR study of valency states in MnFe₂O₄, *Phys. Stat. Sol. A* 40 (1977) K169–K171.
- [105] H. Štěpánková, B. Sedláček, V. Chlan, P. Novák, Z. Šimša, ⁵⁷Fe NMR and spin structure of manganese ferrite, *Phys. Rev. B* 77 (2008) 092416, <https://doi.org/10.1103/PhysRevB.77.092416>.
- [106] Z. Šimša, V.A.M. Brabers, Influence of the degree of inversion on magnetic properties of MnFe₂O₄, *IEEE Trans. Magn.* 11 (1975) 1303–1305, <https://doi.org/10.1109/TMAG.1975.1058861>.
- [107] J.-R. Huang, C. Cheng, Cation and magnetic orders in MnFe₂O₄ from density functional calculations, *J. Appl. Phys.* 113 (2013) 033912, <https://doi.org/10.1063/1.4776771>.
- [108] H. Yasuoka, A. Hirai, T. Shinjo, M. Kiyama, Y. Bando, T. Takada, NMR determination of metal ion distribution in manganese ferrite prepared from aqueous solution, *J. Phys. Soc. Jpn.* 22 (1967) 174–180, <https://doi.org/10.1143/JPSJ.22.174>.
- [109] P.J. van der Zaag, V.A.M. Brabers, M.T. Johnson, A. Noordermeer, P.F. Bongers, Comment on “Particle-size effects on the value of T_C of MnFe₂O₄: Evidence for finite-size scaling”, *Phys. Rev. B* 51 (1995) 12009–12011, <https://doi.org/10.1103/PhysRevB.51.12009>.
- [110] K. Vamvakidis, M. Katsikini, G. Vourlias, M. Angelakeris, E.C. Paloura, C. Dendrinou-Samara, Composition and hydrophilicity control of Mn-doped ferrite (Mn_xFe_{3-x}O₄) nanoparticles induced by polyol differentiation, *Dalton Trans.* 44 (2015) 5396–5406, <https://doi.org/10.1039/C5DT00012E>.
- [111] F.W. Harrison, W.P. Osmond, R.W. Teale, Cation distribution and magnetic moment of manganese ferrite, *Phys. Rev.* 106 (1957) 865–866, <https://doi.org/10.1103/PhysRev.106.865>.
- [112] X. Lasheras, M. Insausti, J.M. de la Fuente, I. Gil de Muro, I. Castellanos-Rubio, L. Marcano, M.L. Fernández-Gubieda, A. Serrano, R. Martín-Rodríguez, E. Garaio, J.A. García, L. Lezama, Mn-doping level dependence on the magnetic response of Mn_xFe_{3-x}O₄ ferrite nanoparticles, *Dalton Trans.* 48 (2019) 11480–11491, <https://doi.org/10.1039/C9DT01620A>.
- [113] U.I. Tromsdorf, N.C. Bigall, M.G. Kaul, O.T. Bruns, M.S. Nikolich, B. Mollwitz, R.A. Sperling, R. Reimer, H. Hohenberg, W.J. Parak, S. Foerster, U. Beisiegel, G. Adam, H. Weller, Size and surface effects on the MRI relaxivity of manganese ferrite nanoparticle contrast agents, *Nano Lett.* 7 (2007) 2422–2427, <https://doi.org/10.1021/nl071099b>.
- [114] J. Lee, J. Yang, S.-B. Seo, H.-J. Ko, J.-S. Suh, Y.-M. Huh, S. Haam, Smart nanoprobe for ultrasensitive detection of breast cancer via magnetic resonance imaging, *Nanotechnology* 19 (2008) 485101, <https://doi.org/10.1088/0957-4484/19/48/485101>.
- [115] D.-H. Kim, H. Zeng, T.C. Ng, C.S. Brazel, T₁ and T₂ relaxivities of succimer-coated MFe₂³⁺O₄ (M=Mn²⁺, Fe²⁺ and Co²⁺) inverse spinel ferrites for potential use as phase-contrast agents in medical MRI, *J. Magn. Magn. Mater.* 321 (2009) 3899–3904, <https://doi.org/10.1016/j.jmmm.2009.07.057>.
- [116] T. Ahmad, Y. Iqbal, H. Bae, I. Rhee, S. Hong, Y. Chang, J. Lee, Relaxivities of hydrogen protons in aqueous solutions of gold-coated manganese ferrite nanoparticles, *J. Korean Phys. Soc.* 62 (2013) 1696–1701, <https://doi.org/10.3938/jkps.62.1696>.
- [117] G. Yang, F. He, R. Lv, S. Gai, Z. Cheng, Y. Dai, P. Yang, A cheap and facile route to synthesize monodisperse magnetic nanocrystals and their application as MRI agents, *Dalton Trans.* 44 (2015) 247–253, <https://doi.org/10.1039/C4DT02425G>.
- [118] Y. Li, X. Zhao, X. Liu, K. Cheng, X. Han, Y. Zhang, H. Min, G. Liu, J. Xu, J. Shi, H. Qin, H. Fan, L. Ren, G. Nie, A bioinspired nanoprobe with multilevel responsive T₁-Weighted MR signal-amplification illuminates ultrasmall metastases, *Adv. Mater.* (2019) 1906799, <https://doi.org/10.1002/adma.201906799>.
- [119] Y. Miao, H. Zhang, X. Liu, A. Ghosal, H. Fan, Q. Xie, J. Cai, J. Jiao, S. Hu, Y. Yang, Composition-tunable ultrasmall manganese ferrite nanoparticles: insights into their in vivo T₁ contrast efficacy, *Theranostics* 9 (2019) 1764–1776, <https://doi.org/10.7150/thno.31233>.
- [120] S. Faraji, G. Dini, M. Zahraei, Polyethylene glycol-coated manganese-ferrite nanoparticles as contrast agents for magnetic resonance imaging, *J. Magn. Magn. Mater.* 475 (2019) 137–145, <https://doi.org/10.1016/j.jmmm.2018.11.097>.
- [121] J. Giri, P. Pradhan, V. Somani, H. Chelawat, S. Chhatre, R. Banerjee, D. Bahadur, Synthesis and characterizations of water-based ferrofluids of substituted ferrites [Fe_{1-x}B_xFe₂O₄, B = Mn, Co (x = 0–1)] for biomedical applications, *J. Magn. Magn. Mater.* 320 (2008) 724–730, <https://doi.org/10.1016/j.jmmm.2007.08.010>.
- [122] L. Yang, L. Ma, J. Xin, A. Li, C. Sun, R. Wei, B.W. Ren, Z. Chen, H. Lin, J. Gao, Composition tunable manganese ferrite nanoparticles for optimized T₂ contrast ability, *Chem. Mater.* 29 (2017) 3038–3047, <https://doi.org/10.1021/acs.chemmater.7b00035>.
- [123] R.V. Upadhyay, K.J. Davies, S. Wells, S.W. Charles, Preparation and characterization of ultra-fine MnFe₂O₄ and Mn_xFe_{1-x}Fe₂O₄ spinel systems: I. particles, *J. Magn. Magn. Mater.* 132 (1994) 249–257, [https://doi.org/10.1016/0304-8853\(94\)90320-4](https://doi.org/10.1016/0304-8853(94)90320-4).
- [124] L. Wang, Q. Wu, S. Tang, J. Zeng, R. Qiao, P. Zhao, Y. Zhang, F. Hu, M. Gao, Ultrasmall PEGylated Mn_xFe_{3-x}O₄ (x = 0–0.34) nanoparticles: effects of Mn(II) doping on T₁- and T₂-weighted magnetic resonance imaging, *RSC Adv.* 3 (2013) 23454–23460, <https://doi.org/10.1039/c3ra43985b>.
- [125] A. Boni, M. Marinone, C. Innocenti, C. Sangregorio, M. Corti, A. Lascialfari, M. Mariani, F. Orsini, G. Poletti, M.F. Casula, Magnetic and relaxometric properties of Mn ferrites, *J. Phys. D: Appl. Phys.* 41 (2008), 134021, <https://doi.org/10.1088/0022-3727/41/13/134021>.
- [126] A. Ereath Beeran, S.S. Nazeer, F. Boniface Fernandez, K. Surendra Muvvala, W. Wunderlich, S. Anil, S. Vellappally, M.S.R. Rao, A. John, R.S. Jayasree, P.R.H. Varma, An aqueous method for the controlled manganese (Mn²⁺) substitution in superparamagnetic iron oxide nanoparticles for contrast enhancement in MRI, *Phys. Chem. Chem. Phys.* 17 (2015) 4609–4619, <https://doi.org/10.1039/C4CP05122J>.
- [127] A. Ereath Beeran, F. Boniface Fernandez, A. John, S.S. Nazeer, R.S. Jayasree, S. Anil, S. Vellappally, A.A.A. Al Kheraif, P.R.H. Varma, Multifunctional nano manganese ferrite ferrofluid for efficient theranostic application, *Colloids Surf. B Biointerfaces* 136 (2015) 1089–1097, <https://doi.org/10.1016/j.colsurfb.2015.11.010>.
- [128] A. Pardo, B. Pelaz, J. Gallo, M. Bañobre-López, W.J. Parak, S. Barbosa, P. del Pino, P. Taboada, Synthesis, characterization, and evaluation of superparamagnetic doped ferrites as potential therapeutic nanotools, *Chem. Mater.* 32 (2020) 2220–2231, <https://doi.org/10.1021/acs.chemmater.9b04848>.

- [129] K. Vamvakidis, D. Sakellari, M. Angelakeris, C. Dendrinos-Samara, Size and compositionally controlled manganese ferrite nanoparticles with enhanced magnetization, *J. Nanopart. Res.* 15 (2013) 1743, <https://doi.org/10.1007/s11051-013-1743-x>.
- [130] J. Amighian, E. Karimzadeh, M. Mozaffari, The effect of Mn²⁺ substitution on magnetic properties of Mn_xFe_{3-x}O₄ nanoparticles prepared by coprecipitation method, *J. Magn. Mater.* 332 (2013) 157–162, <https://doi.org/10.1016/j.jmmm.2012.12.005>.
- [131] O. Kaman, J. Kuličková, V. Herynek, J. Koktan, M. Maryško, T. Dědourková, K. Knížek, Z. Jiráč, Preparation of Mn-Zn ferrite nanoparticles and their silica-coated clusters: Magnetic properties and transverse relaxivity, *J. Magn. Mater.* 427 (2017) 251–257, <https://doi.org/10.1016/j.jmmm.2016.10.095>.
- [132] C. Rath, S. Anand, R.P. Das, K.K. Sahu, S.D. Kulkarni, S.K. Date, N.C. Mishra, Dependence on cation distribution of particle size, lattice parameter, and magnetic properties in nanosize Mn-Zn ferrite, *J. Appl. Phys.* 91 (2002) 2211–2215, <https://doi.org/10.1063/1.1432474>.
- [133] C. Rath, N.C. Mishra, S. Anand, R.P. Das, K.K. Sahu, C. Upadhyaya, H.C. Verma, Appearance of superparamagnetism on heating nanosize Mn_{0.65}Zn_{0.35}Fe₂O₄, *Appl. Phys. Lett.* 76 (2000) 475–477, <https://doi.org/10.1063/1.125792>.
- [134] L.L. Ding, L.C. Xue, Z.Z. Li, S.Q. Li, G.D. Tang, W.H. Qi, L.Q. Wu, X.S. Ge, Study of cation distributions in spinel ferrites M_xMn_{1-x}Fe₂O₄ (M=Zn, Mg, Al), *AIP Adv.* 6 (2016), 105012, <https://doi.org/10.1063/1.4966253>.
- [135] J. Xie, L. Song, G. Chen, Q. Ding, C. Yan, N. Gu, Y. Zhang, C. Yan, S. Wen, F. Zang, High-performance PEGylated Mn-Zn ferrite nanocrystals as a passive-targeted agent for magnetically induced cancer theranostics, *Biomaterials* 35 (2014) 9126–9136, <https://doi.org/10.1016/j.biomaterials.2014.07.019>.
- [136] R. Arulmurugan, B. Jeyadevan, G. Vaidyanathan, S. Senthilnathan, Effect of zinc substitution on Co-Zn and Mn-Zn ferrite nanoparticles prepared by coprecipitation, *J. Magn. Mater.* 288 (2005) 470–477, <https://doi.org/10.1016/j.jmmm.2004.09.138>.
- [137] I. Sharifi, H. Shokrollahi, S. Amiri, Ferrite-based magnetic nanofluids used in hyperthermia applications, *J. Magn. Mater.* 324 (2012) 903–915, <https://doi.org/10.1016/j.jmmm.2011.10.017>.
- [138] A. Hamed, A.G. Fitzgerald, L.Y. Wang, M. Gueorguieva, R. Malik, A. Melzer, Characterisation of Mn_{0.7}Zn_{0.3}Fe₂O₄ nanoparticles prepared by two stage annealing, *Mater. Technol.* 28 (2013) 339–346, <https://doi.org/10.1179/1753555713Y.0000000066>.
- [139] F.A. Cardona, E.S. Urquiza, P.D.L. Presa, S.H. Tobón, U. Pal, P.H. Fraijo, M.J. Yacamán, J.D. Lozada Ramirez, R. Ivkov, A. Angulo-Molina, M.A. Mendez-Rojas, Enhanced magnetic properties and MRI performance of bi-magnetic core-shell nanoparticles, *RSC Adv.* 6 (2016) 77558–77568, <https://doi.org/10.1039/C6RA14265F>.
- [140] Q.L. Vuong, P. Gillis, Y. Gossuin, Monte Carlo simulation and theory of proton NMR transverse relaxation induced by aggregation of magnetic particles used as MRI contrast agents, *J. Magn. Reson.* 212 (2011) 139–148, <https://doi.org/10.1016/j.jmr.2011.06.024>.
- [141] Z. Wang, J. Liu, T. Li, J. Liu, B. Wang, Controlled synthesis of MnFe₂O₄ nanoparticles and Gd complex-based nanocomposites as tunable and enhanced T₁/T₂-weighted MRI contrast agents, *J. Mater. Chem. B* 2 (2014) 4748–4753, <https://doi.org/10.1039/C4TB00342J>.
- [142] Z. Zhao, X. Chi, L. Yang, R. Yang, B.W. Ren, X. Zhu, P. Zhang, J. Gao, Cation exchange of anisotropic-shaped magnetite nanoparticles generates high-relaxivity contrast agents for liver tumor imaging, *Chem. Mater.* 28 (2016) 3497–3506, <https://doi.org/10.1021/acs.chemmater.6b01256>.
- [143] Z. Zhao, C. Sun, J. Bao, L. Yang, R. Wei, J. Cheng, H. Lin, J. Gao, Surface manganese substitution in magnetite nanocrystals enhances T₁ contrast ability by increasing electron spin relaxation, *J. Mater. Chem. B* 6 (2018) 401–413, <https://doi.org/10.1039/c7tb02954c>.
- [144] K.C.-F. Leung, Y.-X.J. Wang, H. Wang, S. Xuan, C.-P. Chak, C.H.K. Cheng, Biological and magnetic contrast evaluation of shape-selective Mn-Fe nanowires, *IEEE Trans. Nanobiosci.* 8 (2009) 192–198, <https://doi.org/10.1021/cm901618m>.
- [145] C.R. Vestal, Z.J. Zhang, Effects of surface coordination chemistry on the magnetic properties of MnFe₂O₄ spinel ferrite nanoparticles, *J. Am. Chem. Soc.* 125 (2003) 9828–9833, <https://doi.org/10.1021/ja035474n>.
- [146] F.H. Martins, F.G. Silva, F.L.O. Paula, J. de A. Gomes, R. Aquino, J. Mestnik-Filho, P. Bonville, F. Porcher, R. Perzynski, J. Depeyrot, Local structure of core-shell MnFe₂O₄-based nanocrystals: cation distribution and valence states of manganese ions, *J. Phys. Chem. C* 121 (2017) 8982–8991, <https://doi.org/10.1021/acs.jpcc.6b09274>.
- [147] W. Zhang, J. Martinelli, J.A. Peters, J.M.A. Van Hengst, H. Bouwmeester, E. Kramer, C.S. Bonnet, F. Szeremeta, E. Tóth, K. Djanashvili, Surface PEG grafting density determines magnetic relaxation properties of Gd-loaded porous nanoparticles for MR imaging applications, *ACS Appl. Mater. Interfaces* 9 (2017) 23458–23465, <https://doi.org/10.1021/acsami.7b05912>.
- [148] B. Sahoo, K.S.P. Devi, S. Dutta, T.K. Maiti, P. Pramanik, D. Dhara, Biocompatible mesoporous silica-coated superparamagnetic manganese ferrite nanoparticles for targeted drug delivery and MR imaging applications, *J. Colloid Interface Sci.* 431 (2014) 31–41, <https://doi.org/10.1016/j.jcis.2014.06.003>.
- [149] D.-H. Kim, D.E. Nikles, C.S. Brazel, Synthesis and characterization of multifunctional chitosan-MnFe₂O₄ nanoparticles for magnetic hyperthermia and drug delivery, *Materials* 3 (2010) 4051–4065, <https://doi.org/10.3390/ma3074051>.
- [150] J.-H. Lee, J.-T. Jang, J.-S. Choi, S.H. Moon, S.-H. Noh, J.-W. Kim, J.-G. Kim, I.-S. Kim, K.I. Park, J. Cheon, Exchange-coupled magnetic nanoparticles for efficient heat induction, *Nat. Nanotechnol.* 6 (2011) 418–422, <https://doi.org/10.1038/nnano.2011.95>.
- [151] T.-J. Yoon, H. Lee, H. Shao, R. Weissleder, Highly magnetic core-shell nanoparticles with a unique magnetization mechanism, *Angew. Chem., Int. Ed.* 50 (2011) 4663–4666, <https://doi.org/10.1002/anie.201100101>.
- [152] Y. Matsumoto, A. Jasanoff, T₂ relaxation induced by clusters of superparamagnetic nanoparticles: Monte Carlo simulations, *Magn. Reson. Imaging* 26 (2008) 994–998, <https://doi.org/10.1016/j.mri.2008.01.039>.
- [153] J.B. Livramento, É. Tóth, A. Sour, A. Borel, A.E. Merbach, R. Ruloff, High relaxivity confined to a small molecular space: a metallostar-based, potential MRI contrast agent, *Angew. Chem., Int. Ed.* 44 (2005) 1480–1484, <https://doi.org/10.1002/anie.200461875>.
- [154] J. Lee, J. Yang, H. Ko, S. Oh, J. Kang, J. Son, K. Lee, S.W. Lee, H.G. Yoon, J.S. Suh, Y. M. Huh, S. Haam, Multifunctional magnetic gold nanocomposites: human epithelial cancer detection via magnetic resonance imaging and localized synchronous therapy, *Adv. Funct. Mater.* 18 (2008) 258–264, <https://doi.org/10.1002/adfm.200700482>.
- [155] O. Kaman, V. Herynek, P. Veverka, L. Kubičková, M. Pashchenko, J. Kuličková, Z. Jiráč, Transverse relaxivity of nanoparticle contrast agents for MRI: different magnetic cores and coatings, *IEEE Trans. Magn.* 54 (2018), 5300405, <https://doi.org/10.1109/tmag.2018.2844253>.
- [156] H.M. Kim, H. Lee, K.S. Hong, M.Y. Cho, M.-H. Sung, H. Poo, Y.T. Lim, Synthesis and high performance of magnetofluorescent polyelectrolyte nanocomposites as MR/near-infrared multimodal cellular imaging nanoprobes, *ACS Nano* 5 (2011) 8230–8240, <https://doi.org/10.1021/nn202912b>.
- [157] J. Leng, J. Li, J. Ren, L. Deng, C. Lin, Star-block copolymer micellar nanocomposites with Mn, Zn-doped nano-ferrite as superparamagnetic MRI contrast agent for tumor imaging, *Mater. Lett.* 152 (2015) 185–188, <https://doi.org/10.1016/j.matlet.2015.03.120>.
- [158] E. Peng, E.S.G. Choo, P. Chandrasekharan, C.-T. Yang, J. Ding, K.-H. Chuang, J.M. Xue, Synthesis of manganese ferrite/graphene oxide nanocomposites for biomedical applications, *Small* 8 (2012) 3620–3630, <https://doi.org/10.1002/smll.201201427>.
- [159] Y. Yang, H. Shi, Y. Wang, B. Shi, L. Guo, S. Yang, H. Wu, D. Wu, Graphene oxide/manganese ferrite nanohybrids for magnetic resonance imaging, photothermal therapy and drug delivery, *J. Biomater. Appl.* 30 (2016) 810–822, <https://doi.org/10.1177/0885328215601926>.
- [160] S.-B. Seo, J. Yang, E.-S. Lee, Y. Jung, K. Kim, S.-Y. Lee, D. Kim, J.-S. Suh, Y.-M. Huh, S. Haam, Nanohybrids via a polycation-based nanocomposite method for dual-mode detection of human mesenchymal stem cells, *J. Mater. Chem.* 18 (2008) 4402–4407, <https://doi.org/10.1039/B804544E>.
- [161] E.S.G. Choo, E. Peng, R. Rajendran, P. Chandrasekharan, C.-T. Yang, J. Ding, K.-H. Chuang, J. Xue, Superparamagnetic nanostructures for off-resonance magnetic resonance spectroscopic imaging, *Adv. Funct. Mater.* 23 (2013) 496–505, <https://doi.org/10.1002/adfm.201200275>.
- [162] A. Ahmad, H. Bae, I. Rhee, Highly stable silica-coated manganese ferrite nanoparticles as high-efficacy T₂ contrast agents for magnetic resonance imaging, *AIP Adv.* 8 (2018), 055019, <https://doi.org/10.1063/1.5027898>.
- [163] Z. Li, S.X. Wang, Q. Sun, H.L. Zhao, H. Lei, M.B. Lan, Z.X. Cheng, X.L. Wang, S.X. Dou, G.Q. Lu, Ultrasmall manganese ferrite nanoparticles as positive contrast agent for magnetic resonance imaging, *Adv. Healthcare Mater.* 2 (2013) 958–964, <https://doi.org/10.1002/adhm.201200340>.
- [164] J.-S. Choi, J.-H. Lee, T.-H. Shin, H.-T. Song, E.Y. Kim, J. Cheon, Self-confirming “AND” logic nanoparticles for fault-free MRI, *J. Am. Chem. Soc.* 132 (2010) 11015–11017, <https://doi.org/10.1021/ja104503g>.
- [165] H. Wang, D.H. Bremner, K. Wu, X. Gong, Q. Fan, X. Xie, H. Zhang, J. Wu, L.-M. Zhu, Platelet membrane biomimetic bufalin-loaded hollow MnO₂ nanoparticles for MRI-guided chemo-chemodynamic combined therapy of cancer, *Chem. Eng. J.* 382 (2020) 122848, <https://doi.org/10.1016/j.cej.2019.122848>.
- [166] L.H. Reddy, J.L. Arias, J. Nicolas, P. Couvreur, Magnetic nanoparticles: design and characterization, toxicity and biocompatibility, pharmaceutical and biomedical applications, *Chem. Rev.* 112 (2012) 5818–5878, <https://doi.org/10.1021/cr300068p>.

Glossary

- CA: Contrast agent
 CPMG: Carr-Purcell-Meiboom-Gill (pulse sequence)
 DOTA: 1,4,7,10-tetraazacyclododecane-1,4,7,10-tetraacetate
 DLS: dynamic light scattering
 DTPA: Diethylenetriamine-N,N,N',N'-pentaacetate
 EELS: electron energy loss spectroscopy
 ICP-OES: Inductively coupled plasma – optical emission spectroscopy
 MAR: motional averaging regime
 MRI: magnetic resonance imaging
 NMR: nuclear magnetic resonance
 NP: nanoparticle
 NPD: neutron powder diffraction
 PRR: partial refocusing regime
 SDR: static dephasing regime

TEM: transmission electron microscopy	T_B : blocking temperature
XAFS: X-ray absorption fine structure	T_C : Curie temperature
XANES: X-ray absorption near edge structure	T_1 : longitudinal relaxation time
XPS: X-ray photoelectron spectroscopy	T_2 : transverse relaxation time
XRD: X-ray powder diffraction	T_2^* : observed time constant of the free induction NMR signal
C_{NP} : number of NPs per m^3	V : volume
d : diameter	γ_H : gyromagnetic ratio of the 1H nucleus
D_L : thickness of dead layer	$\Delta\omega$: the Larmor frequency of water protons at the particle's surface as compared to those at Infinity
H : magnetic field strength	μ : spin only magnetic moment
f : volume fraction of NPs	μ_B : Bohr magneton
i : degree of inversion	μ_0 : the permeability of a vacuum
J_A : Ayant spectral density	μ_{mol} : magnetic moment per formula unit
J_F : Freed spectral density	η : dynamic viscosity
K : anisotropy constant	ρ : density
k_B : Boltzmann constant	σ : magnetization per mass unit
$L(x)$: Langevin function; $L(x) = \coth x - x^{-1}$ with $x = m_{NP}H/k_B T$	τ_B : correlation time of the Brownian rotation
LF : Larmor Frequency	τ_{CP} : half the time interval between successive 180° pulses in a Carr-Purcell-Meiboom-Gill pulse sequence
m_{NP} : magnetization of a nanoparticle	τ_D : diffusion correlation time
M : magnetization per volume unit	τ_L : correlation time defining the border between SDR and PRR
N : number of NPs per kg	τ_N : Néel correlation time
n : number of formula units per NP	ω_H : angular precession frequency of proton
R_1 : longitudinal relaxation rate	ω_S : angular precession frequency of an electron
R_2 : transverse relaxation rate	
R_2^* : observed rate constant of the free induction NMR signal	
T : absolute temperature	